POLITECNICO DI TORINO

Master of Science in Aerospace Engineering

Academic Year 2025-2026

Graduation Session July 2026

Preliminary Design and CFD Assessment of a Heat Exchanger for the Hydrogen-Fuelled Solar Thermal Thruster within the Green SWaP Project

Supervisors:

Prof. Andrea FERRERO
Prof. Angelo CERVONE
Mr. Riccardo CAMBERTONI

Candidate:

Federica CESARI

Abstract

Within the framework of the European Green SWaP (Green Solar-to-propellant Water Propulsion) project, Solar Thermal Propulsion (STP) is proposed as a sustainable propulsion technology for future space applications. The project aims to develop an in-space mobility architecture capable of converting water into hydrogen (H_2) and hydrogen peroxide (H_2O_2) propellants using solar energy.

This thesis focuses on the preliminary design of the Heat Exchanger (HEX) of the 1 N hydrogen-fuelled Solar Thermal Thruster (STT), where Thermal Energy Storage (TES) and Heat Exchanger (HEX) capabilities are integrated within the same component. The objective is to develop a methodology for identifying geometrically feasible HEX configurations, capable of heating hydrogen from 300 K to at least 1130 K while maintaining acceptable pressure losses.

Starting from a near-1D thermal model, a MATLAB configuration-selection tool was developed to explore the design space of a cylindrical HEX with helical flow channels. The number of channels, the channel inner diameter and the helical pitch are used as design variables in this work. After applying geometric feasibility constraints, the model estimates the key thermal and hydraulic performance parameters of each configuration, including the hydrogen outlet temperature, the pressure drop, the Reynolds number, the convective heat transfer coefficient, the wetted area and the overall heat transfer conductance UA. Thermal requirements and engineering constraints are applied to reduce the design space. A Pareto-based screening of the resulting configurations is followed by a local refinement of the most promising region of the Pareto front.

The selected HEX configurations are assessed through steady-state Conjugate Heat Transfer (CHT) CFD simulations performed in ANSYS Fluent, providing a higher-fidelity evaluation of the thermal and hydraulic behaviour of the designs and enabling comparison with the trends predicted by the MATLAB model.

Acknowledgements

I am grateful to my Supervisor, Professor Angelo Cervone, for the opportunity to join TU Delft and work on a challenging and stimulating research project. Above all, I am grateful for the trust he placed in me throughout this experience and for his constant availability whenever needed.

My sincere thanks go to my PhD Assistant Supervisor, Riccardo Cambertoni. I truly appreciated his collaborative approach, which made me feel part of the research team from day one. He always combined the reliability of a supervisor with the openness and spontaneity of a colleague, creating a working environment that was both stimulating and reassuring.

I would also sincerely thank Professor Andrea Ferrero, my supervisor at Politecnico di Torino, for his support throughout the past months. Even before my departure to TU Delft, he was always available for discussions and advice, and throughout the thesis he remained genuinely interested in the progress of the project. Despite the distance, I could always count on his guidance and prompt feedback.

I would also like to thank the members of the Space Engineering Department at TU Delft for creating a welcoming and inspiring research environment.

Finally, I would like to express my deepest gratitude to my family and friends for always being by my side and encouraging me through every challenge, not only throughout my studies, but throughout my life.

The project leading to this work has received funding from the European Union under the European Innovation Council grant agreement N. 101161583. Green SWaP, Green Solar-to-propellant Water Propulsion.

Table of Contents

List of Tables

List of Figures

List of Acronyms

AM Additive Manufacturing 17–19, 50, 73

CEA Chemical Equilibrium with Applications 30

CFD Computational Fluid Dynamics 8, 9, 21, 23, 34, 46, 49, 50, 53, 55, 57, 58, 60–62, 67, 68, 70, 72, 73

CHT Conjugate Heat Transfer 8, 21, 51, 60

CPU Central Processing Unit 59

ECHA European Chemicals Agency 3

EIC European Innovation Council 6

EWT Enhanced Wall Treatment 54, 68

Green SWaP Green Solar-to-Propellant Water Propulsion 6, 8, 9, 12, 16, 17, 19, 21, 26, 28–30, 70, 71

HEX Heat Exchanger 8, 9, 17–19, 21, 23, 25–30, 33–35, 38–40, 46, 49, 50, 58, 68–71, 73

HPC High-Performance Computing 59

ISRU In-Situ Resources Utilization 4, 12

LEO Low Earth Orbit 17, 19

MPI Message Passing Interface 59

NASA National Aeronautics and Space Administration 30

PCM Phase Change Material iv, 16, 17

RAC Receiver Absorber Cavity 17, 19, 28, 29, 49

RCS Reaction Control System 3, 17, 19, 29

REACH Registration, Evaluation, Authorisation and Restriction of Chemicals 3

SST Shear Stress Transport 53, 55, 67

STP Solar Thermal Propulsion iv, 5, 12, 13, 15–18

STT Solar Thermal Thruster 5, 7, 8, 12–14, 16–19, 21, 23, 25, 47, 70, 72, 73

SVHC Substances of Very High Concern 3

TES Thermal Energy Storage 8, 15–17, 19, 30, 49, 72, 73

TPMS Triply Periodic Minimal Surface 18, 73

WEP Water Electrolysis Propulsion 4

List of Symbols

Roman Symbols

A_e	Nozzle exit cross-sectional area $\mathrm{m^2}$
A_{flow}	Flow cross-sectional area $\mathrm{m^2}$
A_{wet}	Wetted heat exchanger area $\mathrm{m^2}$
c_p	Specific heat capacity at constant pressure $\mathrm{J\,kg^{-1}\,K^{-1}}$
C^+	Empirical constant
D_{cavity}	Cavity diameter of the RAC m
D_{helix}	Helix diameter of the HEX channel m
D_{inner}	Inner tube diameter of the HEX channel m
F	Thrust N
f	Darcy-Weisbach friction factor
f_{helix}	Friction factor corrected for helical curvature (Ito)
g_0	Standard gravitational acceleration $\mathrm{m\,s^{-2}}$
h	Convective heat transfer coefficient $\mathrm{W\,m^{-2}\,K^{-1}}$
I_{sp}	Specific impulse s
k	Turbulent kinetic energy $\mathrm{m^2\,s^{-2}}$
k_t	Thermal conductivity $\mathrm{W\,m^{-1}\,K^{-1}}$
k_{VK}	von Kármán constant
L	RAC axial length m
L_{cavity}	Cavity axial length m

$L_{helix,total}$	Total developed individual tube length m
$\mathcal{M}$	Mean molecular weight $\mathrm{kg\,mol^{-1}}$
$\dot{m}_p$	Propellant mass flow rate $\mathrm{kg\,s^{-1}}$
N_{tubes}	Number of HEX channels
Nu	Nusselt number
p	Helical pitch of the HEX channel m
p_a	Ambient fluid pressure Pa
p_c	Chamber pressure Pa
p_e	Nozzle exit pressure Pa
p_{in}	Inlet pressure (boundary condition) Pa
p_{out}	Outlet pressure (boundary condition) Pa
Pr	Prandtl number
$\dot{Q}$	Thermal power delivered to the propellant W
R	Universal gas constant $\mathrm{J\,mol^{-1}\,K^{-1}}$
Re	Reynolds number
R_h	Helix radius m
R_{spec}	Specific gas constant $\mathrm{J\,kg^{-1}\,K^{-1}}$
T_c	Chamber temperature K
$T_{pr,in}$	Propellant inlet temperature K
$T_{pr,out}$	Propellant outlet temperature K
T_{wall}	Wall temperature K
U	Overall heat transfer coefficient $\mathrm{W\,m^{-2}\,K^{-1}}$
u	Flow velocity $\mathrm{m\,s^{-1}}$
UA	Overall heat transfer conductance $\mathrm{W\,K^{-1}}$
u^+	Dimensionless velocity
u_τ	Friction velocity $\mathrm{m\,s^{-1}}$
v_e	Effective exhaust velocity $\mathrm{m\,s^{-1}}$

y	Normal distance from the wall to the first computational grid point m
y^+	Dimensionless wall distance

Greek Symbols

Δp	Pressure drop Pa
ΔT	Temperature difference K
ε	Turbulent dissipation rate $\mathrm{m^2\,s^{-3}}$
γ	Ratio of specific heats
μ	Dynamic viscosity Pa s
ν	Kinematic viscosity of the fluid $\mathrm{m^2\,s^{-1}}$
ω	Specific dissipation rate $\mathrm{s^{-1}}$
ρ	Density $\mathrm{kg\,m^{-3}}$
τ_w	Wall shear stress Pa

Chapter 1

Introduction

1.1 Space Propulsion Systems

Rocket engines generate thrust by accelerating and expelling a propellant carried onboard the vehicle. Unlike air-breathing propulsion systems, they belong to the class of jet propulsion systems that do not depend on atmospheric air and can therefore operate in the vacuum of space [1].

A fundamental distinction in space propulsion is between primary and secondary propulsion, both of which typically rely on rocket propulsion systems. Primary propulsion is used for major trajectory changes, such as launch, orbit insertion, and orbital transfer manoeuvres. Secondary propulsion, on the other hand, supports spacecraft control and operational manoeuvres, including attitude control and station keeping [1].

Historically, the development of space propulsion systems has been driven primarily by the pursuit of high performance, mission reliability, and cost reduction. In recent years, the growing diversity of space missions has introduced new requirements for propulsion technologies. In addition to meeting mission performance requirements, modern propulsion systems are increasingly expected to be cost-effective, environmentally compatible, reusable, and adaptable to a broad range of mission applications. Consequently, the development of next-generation propulsion technologies is no longer guided solely by traditional performance metrics, but also by sustainability and long-term operational efficiency [1], [2].

At the same time, advances in microelectronics and spacecraft technologies have enabled the adoption of small satellites and microsatellites for an increasing number of space applications. Their reduced development costs, shorter development cycles, and operational flexibility have made them attractive platforms for both commercial and scientific missions. As spacecraft dimensions decrease, increasingly stringent constraints are imposed on all onboard subsystems in terms of mass, volume, and power consumption. These constraints challenge the applicability of many conventional propulsion systems and motivate the search for alternative solutions capable of combining efficiency, compactness, and operational flexibility [3].

1.1.1 Propulsive Trade-off

The mass constraints imposed by modern spacecraft, together with the need to reduce the environmental impact of space activities, make propellant utilization a critical aspect of propulsion system design. As a result, the specific impulse (I_{sp}) is commonly adopted as a figure of merit of the performance of any rocket propulsion system. Since a higher specific impulse implies a lower propellant consumption for a given mission requirement, propulsion systems with high I_{sp} are particularly attractive for mass-constrained platforms such as small satellites [1].

In current space missions, chemical and electric propulsion are the most widely adopted technologies. Their characteristics are, however, very different and often lead to opposite design compromises and limitations [1].

Chemical propulsion systems can deliver high thrust levels, and are therefore suitable for primary propulsion functions and rapid orbital manoeuvres. The drawback is their relatively low specific impulse, which results in a high propellant mass requirement, often requiring a large portion of the spacecraft mass to be dedicated to propellant rather than payload [1].

At the opposite end of the spectrum, electric propulsion systems achieve considerably higher specific impulses and therefore lower propellant consumption. This improvement in propellant efficiency comes at the expense of thrust. As a result, electric thrusters usually need to operate for long periods to produce meaningful changes in velocity. They also require a continuous supply of electrical power, which can be difficult to provide on spacecraft with limited resources. These limitations become particularly relevant for small satellites, where the available electrical power, mass, and volume are constrained [1], [4], [5].

Neither conventional chemical propulsion nor electric propulsion fully satisfies the combination of performance, efficiency, compactness, and operational flexibility increasingly required by modern small-spacecraft missions.

This has motivated the investigation of bimodal propulsion architectures. In these configurations, high-thrust chemical propulsion concepts are typically retained for primary orbital manoeuvres, while alternative high-efficiency propulsion concepts are dedicated to secondary propulsion and Reaction Control System (RCS) applications. These solutions have to provide high specific impulse without the power penalties of electric propulsion.

1.1.2 The Push for Green Propulsion

Historically, spacecraft propulsion systems have relied on hydrazine-based propellants, including hydrazine (N_2H_4), monomethylhydrazine (MMH), and unsymmetrical dimethylhydrazine (UDMH). Their widespread use is mainly due to their storability at ambient conditions and, for bipropellant combinations such as MMH/NTO, their hypergolic ignition characteristics, which simplify engine operation and contribute to high system reliability [1], [6], [7].

Despite these advantages, hydrazine and its derivatives present significant drawbacks. These propellants are highly toxic and require strict safety procedures during transportation, storage, fueling, and launch operations. Dedicated handling procedures, protective equipment, contamination-control measures, and specialized ground facilities are necessary to ensure personnel safety, increasing operational complexity and cost [1].

Growing concerns regarding the environmental and health impacts have increased interest in alternative propellants. A turning point occurred in 2011, when the European Chemicals Agency (ECHA) included hydrazine in the list of Substances of Very High Concern (SVHC) under the Registration, Evaluation, Authorisation and Restriction of Chemicals (REACH) regulatory framework. The possibility of future restrictions on its use within Europe accelerated research into safer and more environmentally sustainable propulsion technologies [6], [7].

These efforts contributed to the development of so-called green propellants, which aim to reduce toxicity and simplify ground operations while maintaining competitive propulsion performance. As a result, sustainable propulsion systems have become an important research area in the space sector [6], [7].

1.1.3 Water as a Resource and its Historical Limitations

Among the green propulsion concepts currently being studied, water has attracted interest as a resource for future space missions. Water is not toxic, chemically stable, and widely available, and in addition to its use as a potential propellant source, it can support several spacecraft functions, including life-support systems, radiation shielding, and thermal management. Furthermore, water is considered a key resource for future In-Situ Resources Utilization (ISRU) strategies, allowing resources and propellants to be produced directly in space [6], [7], [8].

One of the first concepts proposed to exploit water for propulsion was Water Electrolysis Propulsion (WEP). In this approach, water is decomposed into hydrogen (H_2) and oxygen (O_2) through electrolysis, and the resulting gases are then used as propellants. However, this approach has some important limitations: the low density of gaseous hydrogen and oxygen requires large storage volumes; in addition the high combustion temperatures associated with stoichiometric hydrogen-oxygen combustion introduce significant challenges for small propulsion systems, often limiting their operation to very low thrust levels. The electrolysis unit also increases the overall system complexity and dry mass [6], [7].

1.1.4 The Bimodal Water-Based Architecture

Researchers have explored alternative water-based propulsion concepts to exploit the advantages of water while avoiding the main limitations of WEP [6], [7]. One promising approach converts water into concentrated hydrogen peroxide (HTP) and gaseous hydrogen (H_2). Unlike oxygen, HTP can be stored as a dense liquid, reducing tank volume required onboard the spacecraft, and improving volumetric efficiency. Furthermore, the decomposition products of HTP are rich in water vapour. This helps lower the combustion temperature when used with hydrogen, reducing the thermal issues typical of hydrogen-oxygen propulsion systems [6], [7], [8].

This approach allows the implementation of a bimodal propulsion architecture.

HTP can be used as oxidizer in a chemical propulsion system for primary manoeuvres, while hydrogen can be used for secondary propulsion functions such as attitude control and station keeping. In this way, the same water-derived resources can support both primary and secondary propulsion requirements within a single spacecraft architecture [6], [7], [8].

However, the use of hydrogen for low-thrust applications remains a challenge. Conventional chemical thrusters would still face the issue of high combustion temperatures, while electric propulsion systems would require significant electrical power and typically lead to long manoeuvre durations.

1.2 Solar Thermal Propulsion (STP)

Among the propulsion technologies proposed for the utilisation of hydrogen, STP is an attractive option. Unlike chemical propulsion, which generates thrust through combustion, and electric propulsion, which uses electrical power to accelerate charged particles, STP uses solar radiation directly as an energy source. Solar energy is collected and concentrated onto a receiver, where it is converted into thermal energy and transferred to a low-molecular-weight propellant (typically hydrogen). The heated propellant is then expanded through a conventional rocket nozzle to generate thrust [1], [5], [9].

Since solar energy is used directly as the heat source, the propellant can reach high temperatures without requiring complex energy conversion processes. This enables STP systems to reach specific impulse values higher than those of chemical propulsion, while maintaining thrust levels well above those typically achievable by electric propulsion. For this reason, STP is a technology that bridges the performance gap between chemical and electric propulsion [4], [5], [10].

The concept of STP was first proposed in the early years of the space exploration. Despite its potential, the development of STP has been limited by the challenges of long-term storage of cryogenic liquid hydrogen in space. The possibility of producing hydrogen directly from water-based architectures offers a way to overcome this limitation and has renewed interest in STP for future space missions. [5].

At system level, a Solar Thermal Thruster (STT) typically consists of three main subsystems (Figure 1.1). First, a solar concentrator collects and focuses the incoming solar radiation. Second, a receiver-absorber cavity transfers the concentrated solar energy to the propellant flowing through the internal heat-exchange structure. Finally, the heated propellant is expanded through a nozzle to generate thrust. The efficiency with which thermal energy is transferred from the receiver to the propellant, influences the achievable propellant temperature and, therefore, the overall performance of the propulsion system [5], [10].

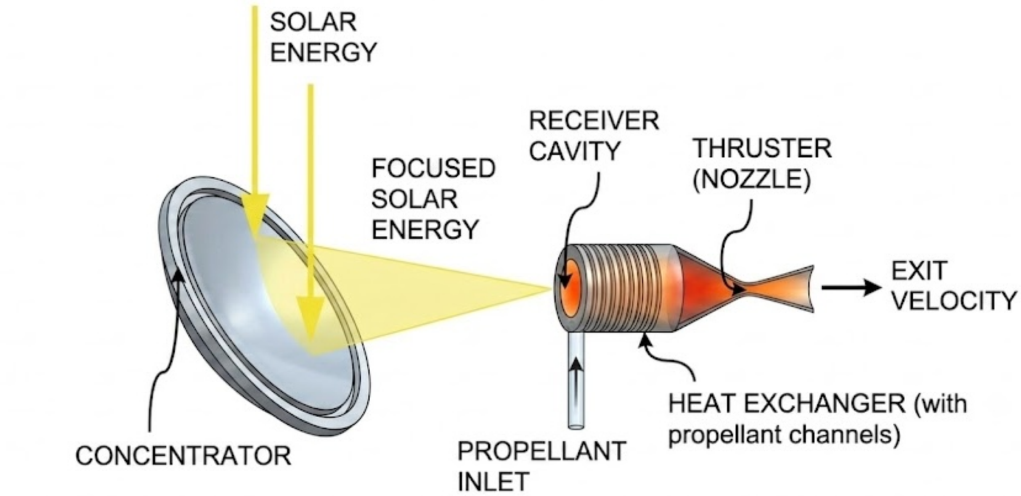

Figure 1.1: Schematic diagram of the principle of STP [6]

1.3 Research Context & Objectives

1.3.1 The Green SWaP Project

The concepts discussed in the previous sections are developed within the Green Solar-to-Propellant Water Propulsion (Green SWaP) project, funded by the European Union, under the European Innovation Council (EIC) Pathfinder programme. The primary objective of the project is to develop a sustainable in-space mobility architecture that uses solar energy to directly convert water into gaseous hydrogen (H_2) and high-concentration hydrogen peroxide (H_2O_2).

Figure 1.2: Green SWaP logo

By producing propellants in space, the proposed architecture reduces dependence on resources launched from Earth, supports water circularity, and promotes a more sustainable use of consumables during space missions. Primary orbital manoeuvres are performed by a 200 N bipropellant (H_2O_2/H_2) chemical thruster, while attitude control and station-keeping are handled by a secondary 1 N STT. Operating exclusively on gaseous hydrogen, the STT is designed to achieve a specific impulse of approximately 500 s, avoiding the electrical power requirements of electric propulsion systems and the combustion of conventional chemical systems [2], [6], [7], [8].

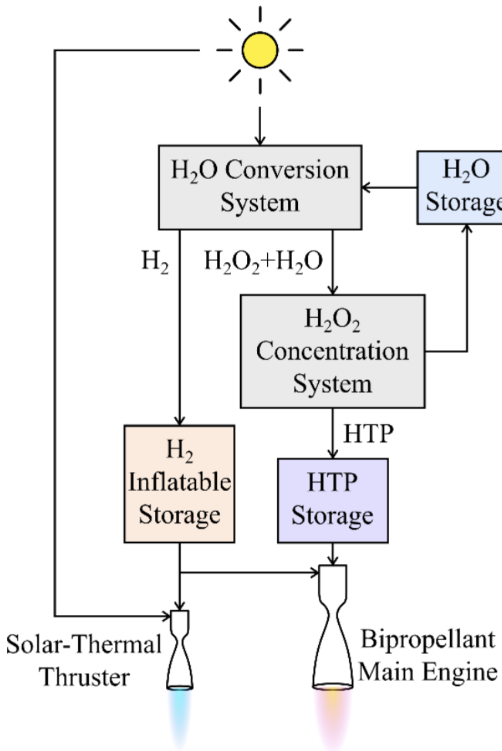

Figure 1.3: Technical scheme of the Green SWaP project architecture [8]

1.3.2 Research Objectives

The Green SWaP project covers the entire technology chain, from solar energy harvesting and propellant conversion to the development of the propulsion systems. This thesis is focused on the thermal core of the secondary propulsion system, the receiver-absorber Heat Exchanger (HEX) of the 1 N STT. As highlighted by Zhang et al. [11], the HEX is the most critical structure within a STT, and its efficiency has a significant influence on the overall performance of the propulsion system.

The main objectives of this thesis are the preliminary design and Computational Fluid Dynamics (CFD) assessment of the receiver-absorber HEX for 1 N STT within the Green SWaP project. Specifically, the component is designed to integrate Thermal Energy Storage (TES) and HEX capabilities within the same architecture. To achieve this, the research activity is divided into the following sub-objectives:

- Development of a MATLAB-based, near-1D thermal model to explore the design space of a cylindrical HEX with helical flow channels.
- Evaluation of the thermal and hydraulic performance of the candidate configurations through parameters such as propellant outlet temperature, pressure drop, and overall heat transfer conductance (UA), followed by a Pareto-based screening and local refinement of configurations capable of heating the propellant from 300 K to at least 1130 K (as discussed in Section 3.2.2).
- Execution of steady-state Conjugate Heat Transfer (CHT) CFD simulations using ANSYS Fluent to assess the thermo-fluid dynamic behaviour of the selected configurations and compare the results with the trends predicted by the MATLAB model.

1.4 Research Questions

In order to achieve these objectives, it is necessary to answer the following research questions:

Q1 How do the main geometric parameters of a helical-tube HEX (number of tubes, tube inner diameter, and helix pitch) affect its thermal and hydraulic performance in a hydrogen-fuelled STT?

Q2 Which HEX configurations can be identified as promising design candidates after applying the Green SWaP thermal requirements and the imposed hydraulic and geometric constraints?

Q3 To what extent do three-dimensional CFD simulations support the thermal and hydraulic performance trends predicted by the preliminary design methodology?

Chapter 2

Literature Review

2.1 Fundamentals of Rocket Propulsion and the Case of STP

According to Sutton and Biblarz [1], the thrust produced by a rocket engine is given by the sum of the momentum and pressure contributions:

$$F = \dot{m}_p \cdot v_e + (p_e - p_a) \cdot A_e \tag{2.1}$$

where $\dot{m}_p$ is the propellant mass flow rate, v_e is the exhaust velocity, p_e and p_a are the exit and ambient fluid pressure, respectively, and A_e is the cross-sectional area at the nozzle exit.

While thrust quantifies the force generated by a propulsion system, the propellant efficiency is expressed through an important figure of merit, the specific impulse (I_{sp}):

$$I_{sp} = \frac{F}{\dot{m} g_0} \tag{2.2}$$

where g_0 is the standard gravitational acceleration. Since the exhaust velocity can be written as:

$$v_e = I_{sp} g_0 \tag{2.3}$$

the specific impulse is generally considered the primary performance metric of a rocket propulsion system.

Applying conservation of specific enthalpy and assuming quasi-steady, adiabatic flow, the energy balance between the chamber and the nozzle exit can be written as:

$$c_p \cdot T_c = c_p \cdot T_e + \frac{v_e^2}{2} \tag{2.4}$$

where c_p is the specific heat of the propellant, T_c is the chamber temperature, and T_e is the nozzle exit temperature.

For an ideal rocket nozzle operating under quasi-one-dimensional isentropic conditions, the exhaust velocity can be further expressed as:

$$v_e = \sqrt{\frac{2\gamma}{\gamma - 1} \frac{R \cdot T_c}{\mathcal{M}} \left[1 - \left(\frac{p_e}{p_c} \right)^{\frac{\gamma-1}{\gamma}} \right]} \tag{2.5}$$

where γ is the specific heat ratio, R is the universal gas constant, T_c is the chamber temperature, $\mathcal{M}$ is the mean molecular weight of the exhaust products, and p_c and p_e are the chamber and exit pressures, respectively.

Substituting Equation 2.3 into Equation 2.5 shows that, for comparable expansion conditions (fixed nozzle geometry and pressure ratio $\frac{p_c}{p_e}$), the ideal specific impulse scales approximately as:

$$I_{sp} \propto \sqrt{\frac{T_c}{\mathcal{M}}} \tag{2.6}$$

This relationship highlights two key parameters that govern propulsion performance: the temperature of the propellant and the molecular weight of the exhaust gases. Propulsion systems capable of heating a low-molecular-weight propellant are expected to achieve higher specific impulse values.

Figure 2.1 illustrates the typical performance ranges of the main rocket propulsion technologies in terms of thrust and specific impulse. Among them, chemical and electric propulsion represent the two dominant solutions currently adopted in space missions. In chemical propulsion, both parameters are determined by the combustion process. High propellant temperatures are limited by material temperature constraints. At the same time, the molecular weight of the exhaust products depends on the selected propellant combination [10]. Electric propulsion follows a different approach. Instead of converting chemical energy into thermal energy, it uses electrical power to accelerate charged particles to high exhaust velocities. This leads to higher specific impulse values than those achievable with chemical propulsion systems. However, the available thrust is related to the onboard power supply and is therefore limited by the spacecraft electrical power budget.

STP has been proposed as an intermediate solution between these two propulsion families. STP uses concentrated solar radiation to heat a propellant before its expansion through a rocket nozzle. This approach enables the use of pure hydrogen, whose exceptionally low molecular weight ($\mathcal{M} \approx 2\ \mathrm{g\,mol^{-1}}$) is particularly advantageous according to Equation 2.6. These systems can therefore combine high specific impulse with moderate thrust levels.

However, STP systems based on ISRU concepts, such as the Green SWaP architecture, must account for propellant impurities. Since hydrogen is produced in orbit from water, the propellant supplied to the STT is not expected to be perfectly pure and may contain small amounts of residual species generated during the conversion process.

Table 2.1 reports the molecular weights of hydrogen, some candidate propellants, and the impurity species expected within the Green SWaP framework.

Substance	**Molecular Weight $\mathcal{M}$ (g/mol)**
Hydrogen (H_2)	2.016
Helium (He)	4.003 Water (H_2O)
18.015	
Nitrogen (N_2)	28.014
Oxygen (O_2)	31.998
Argon (Ar)	39.948

Table 2.1: Molecular weights of candidate propellants and expected impurity species

Because these species are significantly heavier than hydrogen, even small concentrations increase the average molecular weight of the propellant mixture. According to Eq. 2.6, this results in a reduction of the specific impulse.

For the Green SWaP analyses, a conservative hydrogen purity of 98% is assumed as a baseline, with the remaining 2% represented by 1% oxygen and 1% argon.

2.2 Historical Development and Architectures of STT

The origins of STP can be found in the work of Krafft Ehricke in the 1950s, who proposed the use of concentrated solar energy to heat a propellant and generate thrust without relying on chemical combustion [4]. This concept is based on the same principle used in modern STTs: solar radiation is converted into thermal energy, transferred to a propellant, and finally expanded through a nozzle to produce thrust.

In the 1960s and 1970s, several experiments were carried out to evaluate the feasibility of STP. One important example was the work conducted by the Air Force Rocket Propulsion Laboratory (AFRPL), which showed that solar-heated receivers could heat hydrogen to temperatures close to 2300 K. These results confirmed that hydrogen could be an effective propellant for STP systems [4].

As STP technology developed, the design of the receiver-absorber subsystem became a key challenge. The two main approaches explored were direct absorption and indirect absorption.

In direct-absorption, or *windowed*, systems, concentrated solar radiation enters the receiver through a transparent window and heats the propellant directly. Since hydrogen absorbs little radiation, small particles such as tantalum or hafnium carbide are often added to improve energy absorption [9]. This approach can reach high propellant temperatures and specific impulse, but the window is a critical component that can create issues related to high temperatures, sealing, and particle deposits [12], [5]. One of the preferred concepts for direct absorption is the rotating bed concept (Figure 2.2), because it has the highest specific impulse thanks to its retained seed approach.

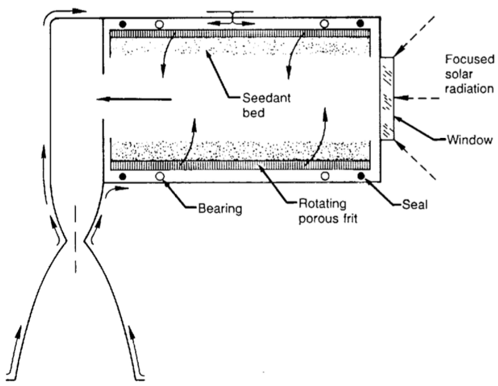

Figure 2.2: Rotating bed concept [9]

Because of these limitations, indirect-absorption, or *windowless*, designs were developed (Figure 2.3). In these systems, concentrated solar radiation is absorbed by the walls of a cavity receiver (usually made of high-temperature metals or ceramics) and then transferred to the propellant flowing through internal channels [9]. Without a transparent window, these systems avoid many of the thermal and structural problems of windowed concepts and are now used in most modern STT designs [10].

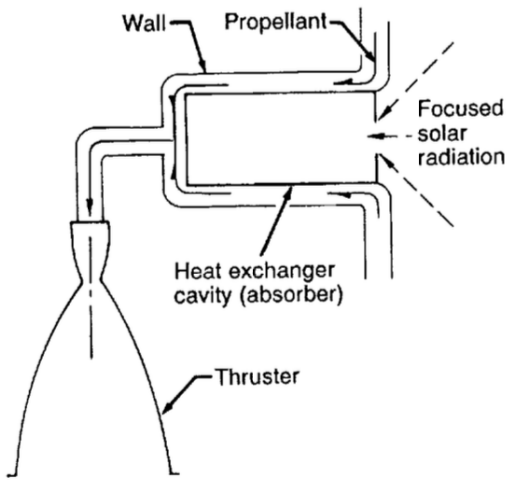

Figure 2.3: Windowless HEX cavity concept [9]

In Figure 2.4 there is a comparison of direct and indirect heating concepts: as said before, the direct absorption concept can achieve higher propellant temperatures and specific impulses, because the propellant absorbs solar energy directly; instead, the indirect concept is limited by wall material temperature. Despite this limitation, both concepts provide a performance improvement compared with conventional chemical propulsion systems.

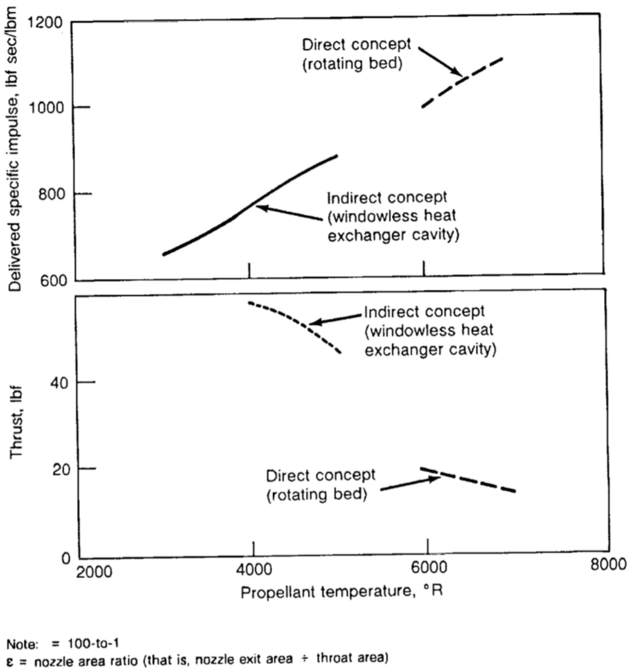

Figure 2.4: Comparison of performance of the indirect and direct absorption concepts for a STT with a collector 100 feet in diameter [9]

An important step in the evolution of STP is represented by the Integrated Solar Upper Stage (ISUS) program, developed by the U.S. Air Force during the 1990s [5]. ISUS was designed not only for STP but also to generate electrical power using the same thermal system. To do this, it included a TES unit that could provide heat for propulsion and for power generation through thermionic conversion [4]. This demonstrated the possibility of combining different spacecraft functions within a single system.

From Ehricke's early concepts to cavity receivers and the ISUS program, STP technology has evolved, providing the foundation for current research, including the Green SWaP project, introduced in Section 1.3.

2.3 TES Integration

An important limitation of STTs is their dependence on continuous solar irradiation. During orbital eclipses or spacecraft attitude manoeuvres that interrupt solar exposure, the available thermal power rapidly decreases, reducing propulsive capability [3].

To mitigate this limitation, several studies have investigated the integration of TES systems within the receiver-absorber assembly. The purpose of TES is to store thermal energy when solar radiation is available and to release it when required. By partially decoupling propulsion operations from solar availability, TES can extend thruster operating time and improve mission flexibility [4].

2.3.1 Early TES Concepts: Sensible Heat Storage

One of the earliest demonstrations of TES integration in STP is the Integrated Solar Upper Stage (ISUS) program. During sunlight exposure, thermal energy was stored within a graphite thermal mass coated with rhenium, increasing material temperature. The stored energy was then transferred to the propellant flowing through internal channels.

This approach, that relied on sensible heat storage, was technically feasible but presented an intrinsic limitation: as the thermal mass discharged, the receiver temperature continuously decreased, leading to a continuous reduction of propellant outlet temperature and thruster performance.

In addition, storing large amounts of energy requires large masses of storage material, increasing the overall system mass and volume [4].

2.3.2 Phase Change Material (PCM) for STP

To overcome the limitations of sensible heat storage, more recent research has investigated latent heat TES based on PCMs. In this approach, thermal energy is stored and released through a phase transition, typically melting and solidification, rather than through a large temperature variation of the storage medium.

High-temperature PCMs such as silicon and boron have been proposed for STP applications, because of their high energy-storage density and elevated phase-change temperatures: they can store larger amounts of energy per unit mass while maintaining an approximately constant temperature during the phase transition process.

As a result, latent heat TES systems can enable thruster operation during eclipse periods while requiring less storage material [3], [4].

2.3.3 TES-Based Architectures in Modern STT Systems

Driven by the need for thrust availability in RCS applications, particularly during the eclipse periods in Low Earth Orbit (LEO), TES has become a key architectural element of several modern STT concepts.

Within the Green SWaP project, TES is integrated within the Receiver Absorber Cavity (RAC), which is responsible for absorbing solar radiation, storing thermal energy, and transferring it to the hydrogen propellant [2], [6].

Consequently, the design of the RAC involves the selection of a suitable storage material, but also the design of the heat-exchange structure. The amount of energy that can be stored and the efficiency with which it can be transferred to the propellant are closely linked.

Recent studies have explored RAC concepts in which the TES region and the HEX are combined within a single structure. In some cases, thanks to Additive Manufacturing (AM) it is possible to realize monolithic designs that reduce thermal contact resistances and avoid issues caused by thermal expansion mismatch between separate components [2].

As a result, the performance of TES-based STTs depends not only on the thermal storage capability of the selected material, but also on the thermal-hydraulic behaviour of the HEX. Maximizing heat transfer while maintaining acceptable pressure losses becomes a key design challenge. For this reason, the heat-exchanger architectures proposed in the literature are reviewed in the following section.

2.4 HEX Design in STT

The HEX plays a key role in the performance of STTs, as it determines how effectively thermal energy is transferred to the propellant. Different architectures have been proposed to enhance heat transfer while limiting pressure losses and system mass. This section reviews the main concepts investigated for STT applications.

2.4.1 Tubular and Helical Heat Exchanger Architectures

Early STT concepts relied on tubular receiver configurations in which the propellant flowed through channels embedded within the receiver structure. Among the different solutions proposed in the literature, helical channels remain one of the most common approaches due to their simple geometry and favourable thermal-hydraulic characteristics [12].

Compared with straight tubes, helical channels generate centrifugal forces that induce secondary flow, known as Dean vortices. These vortices enhance radial mixing and heat transfer between the channel wall and the propellant [13], [14].

As a result, helical geometries can provide higher heat-transfer rates than straight channels while maintaining a compact structure. This, in addition to their relatively simple manufacturing, made them a common baseline solution for STT applications [15].

2.4.2 Compact and Additively Manufactured Architectures

The increasing demand for compact spacecraft has motivated the development of HEXs with higher surface-area-to-volume ratios.

One approach is represented by platelet HEXs, which consist of stacking metallic plates containing micro-channels. These architectures allow an increase in heat-transfer areas within a limited volume and have been studied for high-temperature STP applications [10], [11].

More recently, AM has enabled the realization of complex internal geometries, including lattice structures and Triply Periodic Minimal Surface (TPMS) architectures, such as gyroid and diamond topologies [16], [15].

These designs offer high surface-area-to-volume ratios and can improve heat-transfer performance while maintaining acceptable pressure losses [17]. However, their geometric complexity also complicates their thermal-hydraulic behaviour under STT operating conditions. It remains an active area of research [18].

Advances in AM have enabled the realization of monolithic RAC designs that integrate TES and HEX functionalities within a single component [2], [6].

This design philosophy is currently being investigated within the Green SWaP project for hydrogen-fuelled STTs intended for RCS applications in LEO [18].

As a proof of concept, a preliminary resin prototype of the integrated architecture was produced through AM (Figure 2.5). The prototype includes a plenum, a helical-channel HEX, and a nozzle (designed for atmospheric conditions). It is not intended for functional testing, but for providing a demonstration of the geometric feasibility of the integrated design.

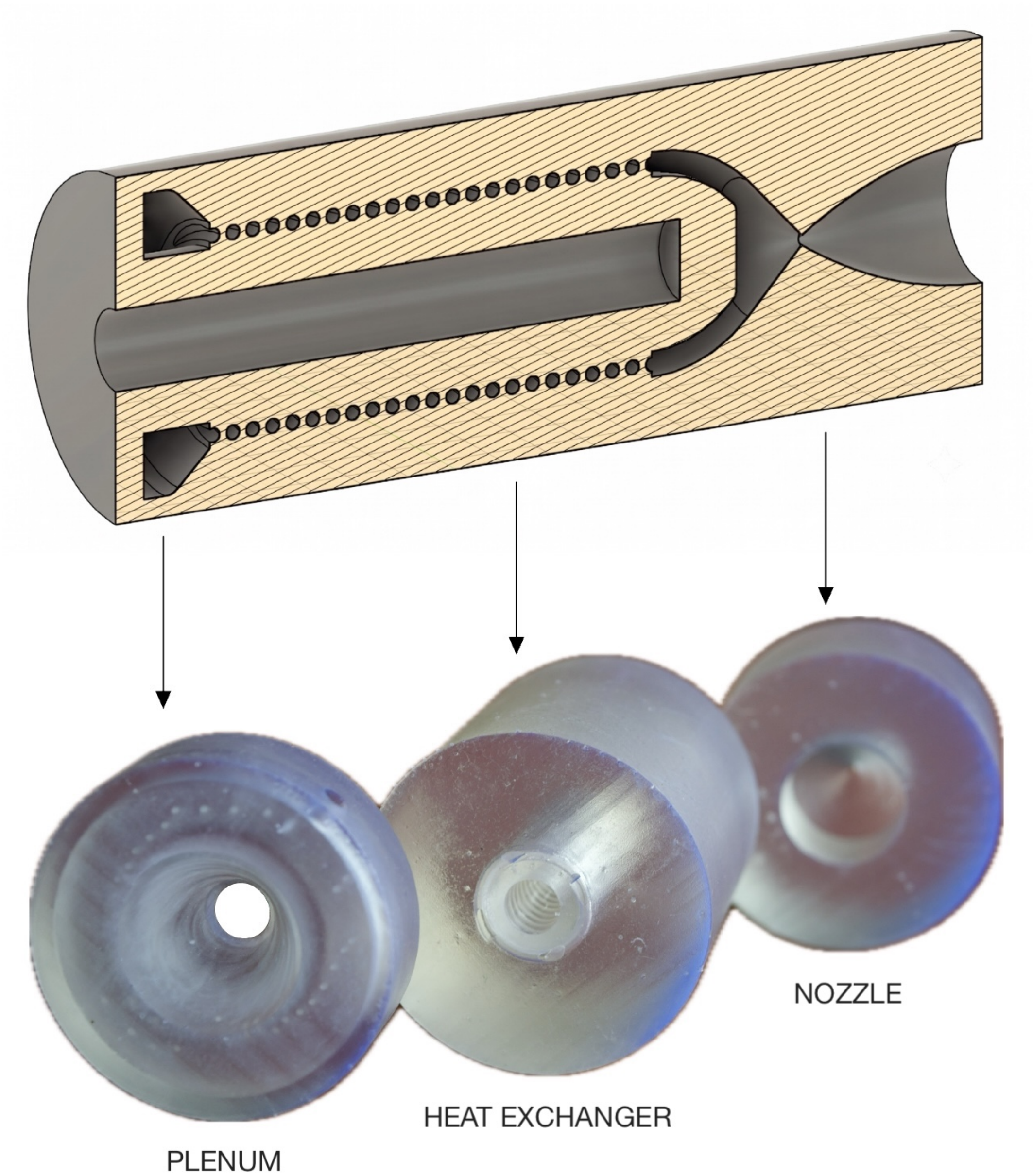

Figure 2.5: Preliminary resin prototype of the helical-channel HEX manufactured through additive manufacturing

2.4.3 Motivation of the Present Work

The literature proposes a wide range of HEX architectures for STTs, from classical helical channels to advanced additively manufactured structures. Despite these developments, helical configurations remain attractive because of their good compromise between simplicity, compactness, and thermal-hydraulic performance.

For this reason, the present work focuses on the preliminary design and CFD assessment of a compact helical HEX, developed within the Green SWaP project.

The objective is to explore the influence of the main geometric parameters on HEX thermal-hydraulic performance and to assess the validity of a preliminary design methodology through higher-fidelity CHT simulations.

Engine Type	Specific Impulse[a] (sec)	Maximum Temperature (°C)	Thrust-to-Weight Ratio[b]	Propulsion Duration	Specific Power[c] (kW/kg)	Typical Working Fluid	Status of Technology
Chemical—solid or liquid bipropellant, or hybrid	200–468	2500–4100	10^{-2}–100	Seconds to a few minutes	10^{-1}–10^{3}	Liquid or solid propellants	Flight proven
Liquid monopropellant	194–223	600–800	10^{-1}–10^{-2}	Seconds to minutes	0.02–200	N_2H_4	Flight proven
Resistojet	150–300	2900	10^{-2}–10^{-4}	Days	10^{-3}–10^{-1}	H_2, N_2H_4	Flight proven
Arc heating—electrothermal	280–800	20,000	10^{-4}–10^{-2}	Days	10^{-3}–1	N_2H_4, H_2, NH_3	Flight proven
Electromagnetic including pulsed plasma (PP)	700–2500	—	10^{-6}–10^{-4}	Weeks	10^{-3}–1	H_2 Solid for PP	Flight proven
Hall effect	1220–2150	—	10^{-4}	Weeks	10^{-1}–5×10^{-1}	Xenon	Flight proven
Ion—electrostatic	1310–7650	—	10^{-6}–10^{-4}	Months, years	10^{-3}–1	Xenon	Flight proven
Solar heating	400–700	1300	10^{-3}–10^{-2}	Days	10^{-2}–1	H_2	In development

[a] At $p_1 = 1000$ psia and optimum gas expansion at sea level ($p_2 = p_3 = 14.7$ psia).
[b] Ratio of thrust force to full propulsion system sea level weight (with propellants, but without payload).
[c] Kinetic power per unit exhaust mass flow.

Figure 2.1: Ranges of typical performance parameters for various rocket propulsion systems [1]

Chapter 3

HEX Design Methodology

3.1 Overall Design Workflow

The design of the STT HEX combines a near-1D preliminary design framework with higher-fidelity CFD simulations.

As illustrated in Figure 3.1, the workflow starts with the definition of the design space and the generation of candidate HEX geometries. A MATLAB-based configuration-selection tool was developed to explore the design space and to evaluate a large number of candidate configurations, through a near-1D thermal-hydraulic model at a relatively low computational cost. Thermal, hydraulic, and geometric requirements were subsequently applied to identify representative configurations for CFD analysis.

Higher-fidelity simulations were finally performed to investigate the thermo-fluid dynamic behaviour of the selected configurations and to evaluate the effect of the main geometrical parameters on their performance.

The following sections describe each stage of the methodology, including the problem definition, the near-1D numerical framework, the design space exploration process, and the selection strategy adopted for the CFD analysis.

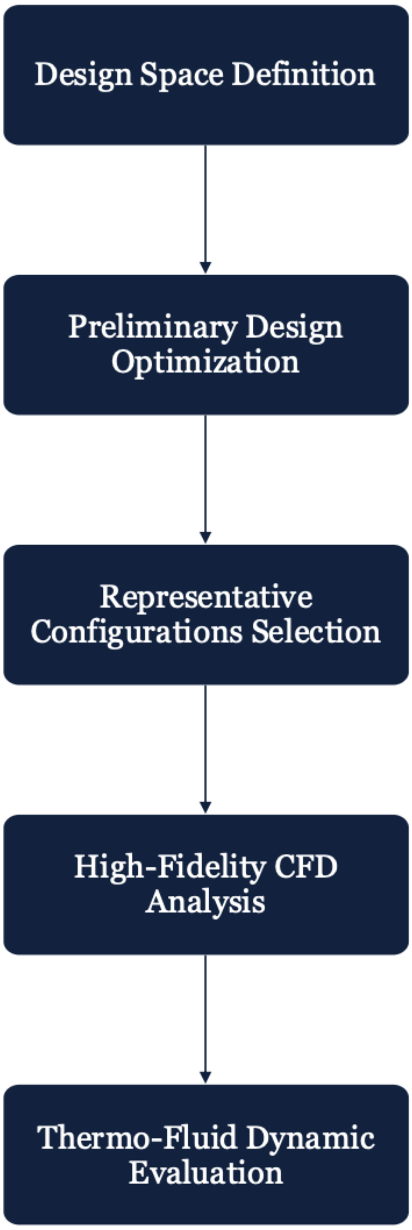

Figure 3.1: Overall workflow

3.2 Problem Definition

3.2.1 Design Objective

The aim of this work is the design and assessment of a compact helical HEX for a hydrogen-fuelled STT. The HEX transfers thermal energy from the receiver to the hydrogen propellant before its expansion through the nozzle.

The design objective is to increase the propellant temperature from the inlet condition to at least the target value of 1130 K (as discussed in Section 3.2.2) at the nozzle inlet, while limiting pressure losses and satisfying the geometrical constraints imposed by the reference thruster architecture.

3.2.2 Mission Driven Requirements & Operating Conditions

The operating conditions adopted throughout the design process are summarized in Table 3.1. These values are representative of the reference STT configuration considered in this work [18].

Parameter	**Value**
Specific impulse (I_{sp})	500 s
Thrust (F)	1 N
Hydrogen inlet temperature ($T_{pr,in}$)	300 K
Hydrogen target outlet temperature ($T_{pr,out}$)	1130 K
Wall temperature (T_{wall})	1400 K
Chamber pressure (p_c)	5 bar
Propellant mass flow rate ($\dot{m}_p$)	0.177 g/s
Cavity diameter (D_{cavity})	10 mm
HEX length (L)	56 mm

Table 3.1: Mission-derived STT and HEX requirements

The target outlet temperature of 1130 K represents the primary thermal requirement for the HEX. This value is derived from the mission requirement to achieve a specific impulse I_{sp} of 500 s, since according to Eq. 2.6, the achievable specific impulse is directly proportional to the square root of the chamber temperature.

Considering a 98% hydrogen purity baseline (with the remaining 2% composed of 1% argon and 1% oxygen residuals from the conversion process (Section 2.1)) and a 10% performance margin for nozzle expansion losses (primary loss mechanisms: non-ideal pressure matching at the nozzle exit, flow divergence in conical nozzles, viscous boundary-layer friction along the nozzle walls, chemical non-equilibrium in the combustion chamber [1], [19]), the required chamber temperature must fall within the 800–1200 K range. Configurations unable to reach this 1130 K threshold were excluded from further analysis.

A constant wall temperature of 1400 K was assumed throughout the analysis, consistently with the steady-state approach adopted in this work. This value provides a conservative 80% convective heat transfer efficiency margin to reach the target fluid temperature. Under this assumption, the receiver acts as a thermal energy reservoir, and the wall temperature can be imposed as a fixed thermal boundary condition.

The chamber pressure of 5 bar and the mass flow rate of 0.177 g/s are defined by the nominal operating conditions required to generate 1 N of thrust. Based on Eq. 2.2, for a target specific impulse and thrust, the theoretical propellant mass flow rate is constrained. It is evaluated within a ±15% band ranging from 0.17 to 0.23 g/s, and the lower bound of 0.177 g/s is selected for the present work.

The hydrogen inlet temperature is set to 300 K, which represents the expected feed temperature from the upstream and storage subsystem.

Finally, the cavity diameter of 10 mm is set as a geometric constraint. This value was derived from reference optical ray-tracing analyses performed for the Green SWaP project [18]. This dimension represents the optimal trade-off to capture the focal spot of the solar concentrator while accommodating mirror slope errors and pointing inaccuracies [20].

3.2.3 Design Variables

The preliminary design exploration was performed by considering three geometrical parameters as design variables: the number of helical channels N_{tubes}, the helical pitch p, and the inner tube diameter D_{inner} (Figure 3.2). These variables define the geometry of the helical HEX and were selected because they directly affect its thermal and hydraulic performance.

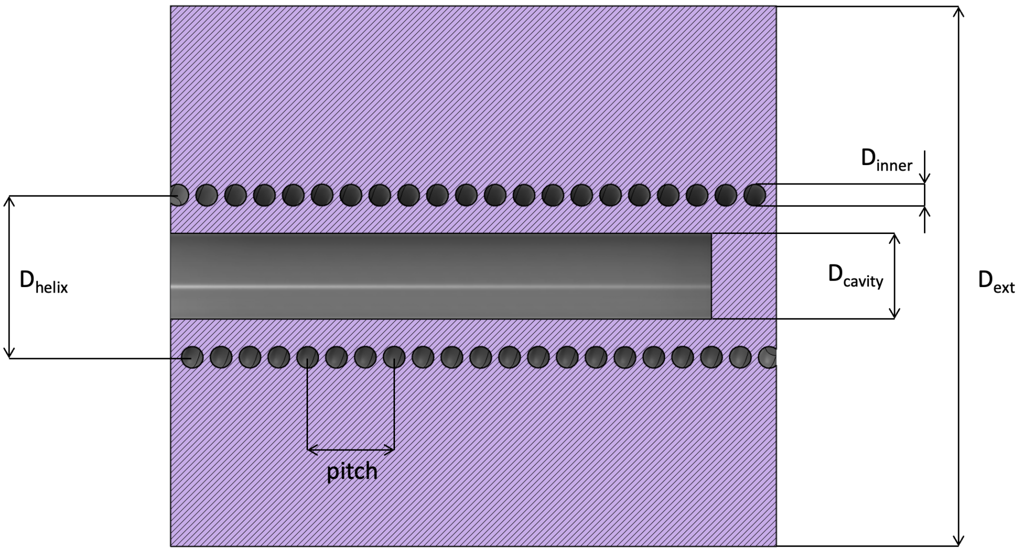

Figure 3.2: Geometrical parameters for a configuration with $N_{tubes} = 3$

The range of values considered for each variable is reported in Table 3.2. The combination of the selected values of N_{tubes}, p, and D_{inner} generated a total of 96 candidate configurations, which were evaluated using the near-1D numerical model described in Section 3.3 and a MATLAB configuration-selection tool.

Design Variable	**Symbol**	**Values**
Number of helical channels	N_{tubes}	$1, 2, 3, 4, 6, 8$
Helical pitch [mm]	p	$5, 8, 10, 15$
Inner tube diameter [mm]	D_{inner}	$1, 1.2, 1.4, 2$

Table 3.2: Range of values considered for each design variable

3.2.4 Design Challenges

The design of the HEX involves the balance of thermal performance, pressure losses, and compactness.

Increasing the heat transfer area or extending the flow path generally improves the thermal energy transferred to the propellant, according to Eqs. (3.15) and

(3.16). However, these modifications also tend to increase pressure losses, according to the Darcy-Weisbach relation (Eq. 3.5), and may reduce the overall compactness of the system. At the same time, shorter flow paths or smaller heat transfer surfaces may not provide sufficient heating of the propellant.

For this reason, the design cannot be driven only by thermal performance. Pressure losses and geometric compactness must also be considered when comparing different solutions. The design problem can therefore be viewed as a multi-objective thermal-hydraulic design task, where different configurations offer different trade-offs between outlet temperature, pressure losses and compactness.

3.3 Near-1D numerical framework

A near-1D Matlab model was used to evaluate the thermal and hydraulic performance of a given HEX configuration.

The geometrical inputs of the model are the design variables introduced in Section 3.2.3: the number of channels N_{tubes}, the helical pitch p, and the inner tube diameter D_{inner}. The thermal and flow boundary conditions are those reported in Table 3.1.

To better understand the role of the model within the Green SWaP project, it is useful to describe the complete operational cycle of the thruster. In reality, the thermal behaviour of the RAC is transient and is characterized by three sequential phases (Figure 3.3), defined as follows [18]:

Phase 1: Pre-heating Phase This phase occurs during the sunlit arc of the orbit, which lasts around 60 minutes in the reference Sun-Synchronous Orbit (SSO). During this period, the solar concentrator focuses solar radiation into the RAC cavity. The core material acts as a thermal battery, absorbing the concentrated solar power and storing it as sensible heat. No propellant flows through the system during this phase. A thermal control system regulates the input power to ensure that the RAC reaches the required wall temperature before the firing phase; at the same time it has to keep the material temperature below its maximum operational limits.

Phase 2: Propellant Heating Phase (Firing Phase) This phase is designed for a maximum firing duration of 20 seconds, to satisfy the RCS slew manoeuvre requirements. Gaseous hydrogen enters the helical channels of the HEX at 300 K and absorbs the thermal energy stored within the RAC. As heat is transferred to the propellant, the temperature of the storage material gradually decreases. This thermal depletion reflects the progressive discharge of the thermal energy stored in the receiver during the firing.

Phase 3: Passive Cooling Phase Following the firing, or during the orbital eclipse periods (which last around 30 minutes), the RAC continues to lose heat to the surrounding space environment. In the absence of solar input, the system slowly loses heat to the surrounding space environment, primarily through thermal radiation. Thermal insulation helps minimize heat losses, allowing the RAC to keep enough stored energy for possible thrust operations during the eclipse period.

Figure 3.3: Phases of the thermal model

The complete thermal model developed within the Green SWaP project describes the interaction between these three phases and is used to assess the thermal behaviour of the thruster over repeated orbital cycles. However, the objective of the present work is not the analysis of the TES system, but the preliminary design of the HEX. For this reason, only the propellant heating phase is considered in the present study.

Within the Green SWaP framework, the firing phase can be evaluated through two modelling approaches: (i) a quasi-steady axial marching model with local thermal equilibrium iterations, and (ii) a fully transient thermal-depletion model, which accounts for the progressive cooling of the RAC. Since the goal of the present configuration-selection tool is the rapid exploration of the design space, the quasi-steady axial marching approach is adopted. This allows the influence of the geometrical parameters on the HEX thermal and hydraulic performance to be investigated independently of the transient thermal response of the TES material.

Although the model is solved iteratively along the axial direction of the HEX, the governing relations are presented according to the main output parameters. This structure shows how the design variables influence the thermal and hydraulic performance of the different configurations.

3.3.1 Model Assumptions and Fluid Properties

The model is based on a near one-dimensional representation of the flow inside the helical channels.

The preliminary sizing methodology implemented in MATLAB was developed considering a TES system. TES systems generally prefer materials with high c_p, as they allow the storage of larger amounts of thermal energy, for a given m and ΔT. For this reason, graphite was adopted as reference material, consistently with the concepts discussed in the literature (Section 2.3).

Moving to the fluid, although hydrogen is the propellant considered in this work, the subscript pr is used in the formulation of the model to keep it general. The hydrogen properties adopted are reported in Table 3.3. These values were derived from the reference analyses of the Green SWaP project [18], where they were estimated using the National Aeronautics and Space Administration (NASA) Chemical Equilibrium with Applications (CEA) tool [21].

Table 3.3: Hydrogen properties adopted in the near-1D model

Property	Symbol	Value
Specific gas constant	R_{spec}	4124 J kg^{-1} K^{-1}
Specific heat capacity	c_p	14310 J kg^{-1} K^{-1}
Dynamic viscosity	μ	8.76×10^{-6} kg m^{-1} s^{-1}
Thermal conductivity	k_f	0.180 W m^{-1} K^{-1}
Prandtl number	Pr	0.6964

3.3.2 Flow Regime and Reynolds Number

For each configuration, the flow area available to the propellant is

$$A_{flow} = N_{tubes} \frac{\pi \cdot D_{inner}^2}{4} \tag{3.1}$$

Assuming ideal-gas behaviour, the propellant density is estimated as

$$\rho_{pr} = \frac{p_c}{R_{spec} \cdot T_{pr}} \tag{3.2}$$

from which the average flow velocity is obtained:

$$u = \frac{\dot{m}}{\rho_{pr} \cdot A_{flow}} \tag{3.3}$$

The Reynolds number is evaluated using the hydraulic diameter as the characteristic length, which coincides with the tube inner diameter D_{inner} in the case of flow developing inside circular channels:

$$Re = \frac{\rho_{pr} \cdot u \cdot D_{inner}}{\mu_{pr}} \tag{3.4}$$

Since the propellant properties are kept constant and the velocity is based on the average flow through the channels, this quantity is used as a representative Reynolds number for each configuration.

3.3.3 Pressure Drop Estimation

The local pressure drop is calculated using the Darcy-Weisbach equation

$$dp = -\frac{f_{helix}}{2} \cdot \rho_{pr} \cdot u^2 \cdot \frac{dz}{D_{inner}} \tag{3.5}$$

where the Friction Factor is evaluated according to the flow regime (Hagen-Poiseuille relation for laminar flow and the Blasius correlation for turbulent flow)

$$f = \begin{cases} 0.3164 \cdot Re^{-0.25} & Re \geq 2300 \quad \textit{(Blausius)} \\ \dfrac{64}{Re} & Re < 2300 \quad \textit{(Hagen-Poiseuille)} \end{cases} \tag{3.6}$$

Because of the helical channels, the friction factor is corrected using the Ito correlation in order to account for curvature effects

$$f_{helix} = f \cdot \left(1 + 3.5\sqrt{\frac{D_{inner}}{2R_h}}\right) \tag{3.7}$$

where the helix curvature radius is defined as

$$R_h = \frac{D_{helix}}{2} \tag{3.8}$$

3.3.4 Heat Transfer Coefficient

The convective heat transfer coefficient is estimated through the Nusselt number. Given the definition of Reynolds number (3.4) and Prandtl number

$$Pr = \frac{c_{p_{pr}} \cdot \mu_{pr}}{k_{f,pr}} \tag{3.9}$$

for turbulent conditions, the Dittus-Boelter correlation is adopted

$$Nu = 0.023 \cdot Re^{0.8} \cdot Pr^{0.4} \tag{3.10}$$

while, for laminar flow a constant value of

$$Nu = 4.36 \tag{3.11}$$

is assumed. The Dittus–Boelter correlation was adopted as the baseline approach for the present work. The sensitivity of the results to the selected correlation is discussed in Section 3.5.

The heat transfer coefficient is therefore obtained from

$$h = \frac{Nu \cdot k_{pr}}{D_{inner}} \tag{3.12}$$

3.3.5 Wetted Area and Overall Conductance

The wetted area A_{wet} represents the internal tube surface in contact with propellant and therefore the area available for convective heat transfer. It is calculated from the total developed length of the helical channels. For a helix radius

$$R_c = \frac{D_{helix}}{2} \tag{3.13}$$

the total developed length of one helical channel is

$$L_{helix,total} = \frac{L}{p} \cdot \sqrt{(2\pi R_c)^2 + p^2} \tag{3.14}$$

The total wetted area available for convective heat transfer is then

$$A_{wet} = \pi \cdot D_{inner} \cdot L_{helix,total} \cdot N_{tubes} \tag{3.15}$$

Finally, the overall heat transfer conductance expressed through the product

$$UA = hA_{wet}. \tag{3.16}$$

3.3.6 Outlet Temperature Calculation

The outlet propellant temperature is determined from the heat exchanged between the HEX wall and the propellant. The heat-transfer rate is expressed as

$$\dot{Q}_{pr} = hA_{wet}\left(T_{wall} - T_{pr}\right) \tag{3.17}$$

The corresponding temperature increase is obtained from the energy balance

$$\dot{Q}_{pr} = \dot{m}c_{p,pr}\Delta T = \dot{m}c_{p,pr}(T_{pr,out} - T_{pr,in}) \rightarrow \Delta T = \frac{\dot{Q}_{pr}}{\dot{m}c_{p,pr}} \tag{3.18}$$

The heating process is evaluated along the axial direction of the HEX, in order to estimate the propellant temperature profile and the outlet temperature.

3.3.7 Model Outputs

For each configuration, the model returns the output parameters summarized in Table 3.4.

Output	Symbol
Outlet Propellant Temperature	$T_{out,pr}$
Pressure Drop	Δp
Mean Reynolds Number	Re_{mean}
Convective Heat Transfer Coefficient	h
Wetted Area	A_{wet}
Overall Heat Transfer Conductance	UA

Table 3.4: Model output parameters

3.4 Design Space Exploration and Candidates Selection

The numerical model described in Section 3.3 was used to explore the design space defined by the selected geometrical variables and identify representative HEX configurations for the subsequent CFD analysis.

The exploration process consisted of four main steps. First, all possible combinations of the selected design variables were generated and evaluated using the model. Second, a set of geometric, thermal and hydraulic feasibility constraints was applied to reduce the number of candidate configurations. Third, a Pareto-based analysis was performed to identify the most promising design solutions. Finally, a local refinement of the design space was carried out to improve the resolution of the Pareto region and support the selection of representative CFD configurations.

3.4.1 TES-Based Design Exploration

The preliminary exploration was performed by evaluating all possible combinations of the design variables introduced in Section 3.2.3. The resulting design space consisted of 96 candidate configurations.

For each configuration, the model computed the thermal and hydraulic quantities described in Section 3.3: the outlet propellant temperature $T_{out,pr}$, the pressure drop Δp, the mean Reynolds number Re_{mean}, the heat transfer coefficient h, the wetted area A_{wet} and the overall heat transfer conductance expressed through the product UA.

Influence of Design Variables

To preliminarily understand the design space, the influence of the main geometric parameters on the thermal and hydraulic performance of the HEX was analysed.

Figure 3.4 shows the variation of $T_{out,pr}$ with N_{tubes} for different combinations of p and D_{inner}. In general, increasing N_{tubes} improves the thermal performance of the HEX, as the available wet area A_{wet} increases (Eq. 3.15). This increase in $T_{out,pr}$ is evident for small D_{inner} but for large D_{inner} the trend changes.

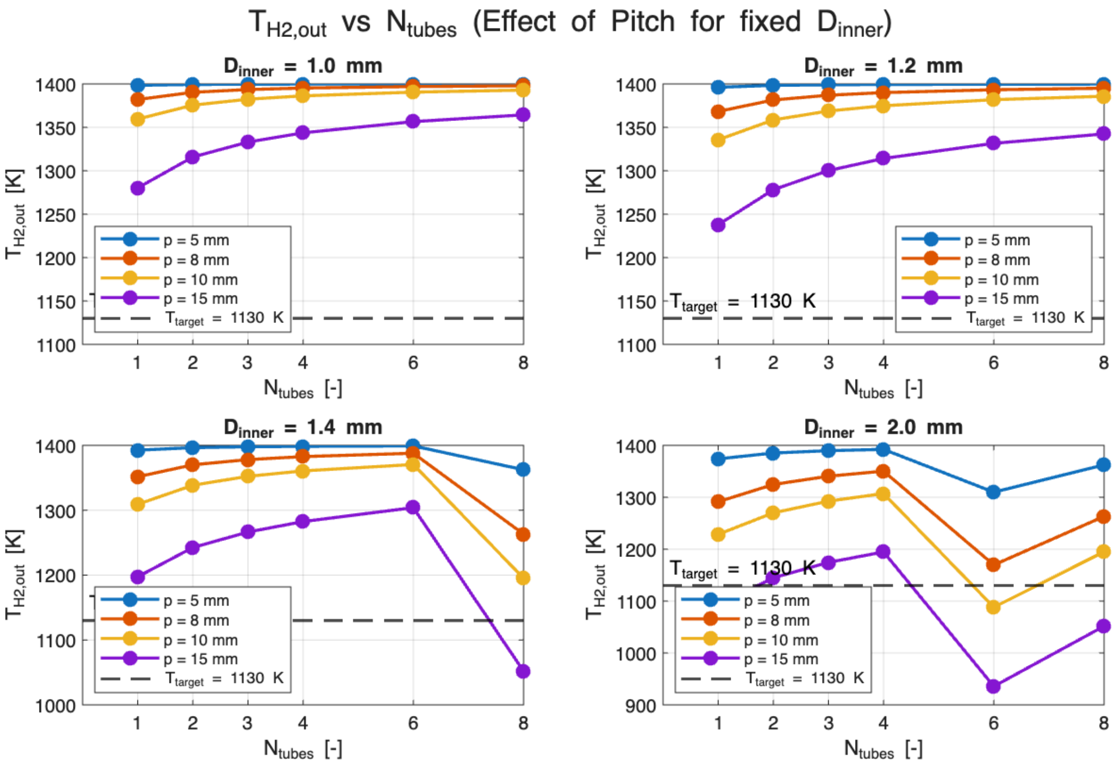

Figure 3.4: Effect of the number of channels on the outlet propellant temperature for different pitch values and tube diameters

Figure 3.5 reports the same analysis for a fixed pitch of 10 mm and variable D_{inner}. Configurations with larger D_{inner} show an earlier drop in $T_{out,pr}$. The decrease appears at lower values of N_{tubes} as the D_{inner} increases.

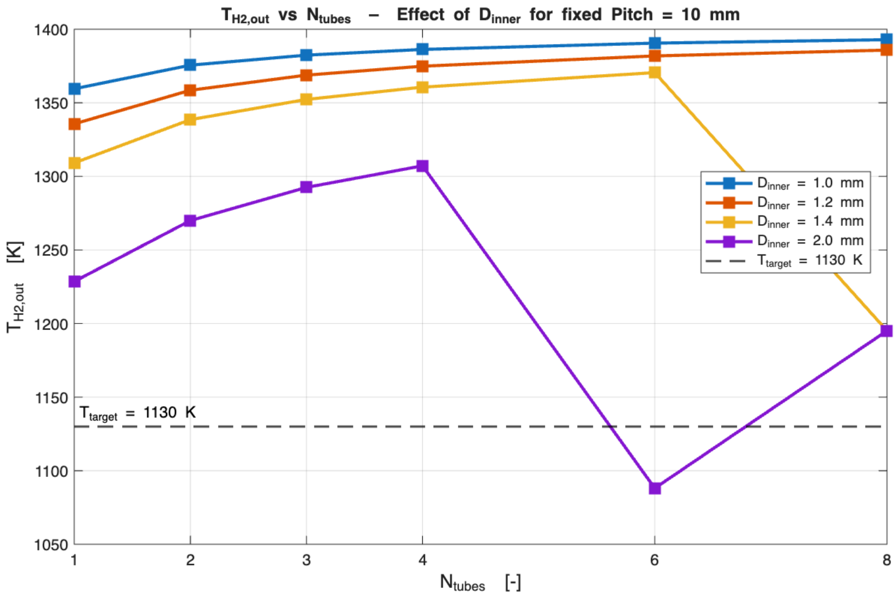

Figure 3.5: Outlet propellant temperature as a function of the number of channels for different tube diameters at a fixed pitch

To better understand these trends, Figure 3.6 compares the $T_{out,pr}$, Re_{mean} and UA for a fixed geometry. Increasing N_{tubes} leads to a larger total flow area (Eq. 3.1), reducing the average flow velocity (Eq. 3.3) and the Reynolds number (Eq. 3.4). This tends to reduce the convective heat-transfer coefficient (Eq. 3.12). At the same time, the additional channels increase the wetted area for heat transfer (Eq. 3.15). As a result, the larger heat-transfer area can compensate for the lower convective heat transfer coefficient. This leads to a higher UA (Eq. 3.16) and explains why the $T_{out,pr}$ can still increase despite the decrease in Re_{mean}.

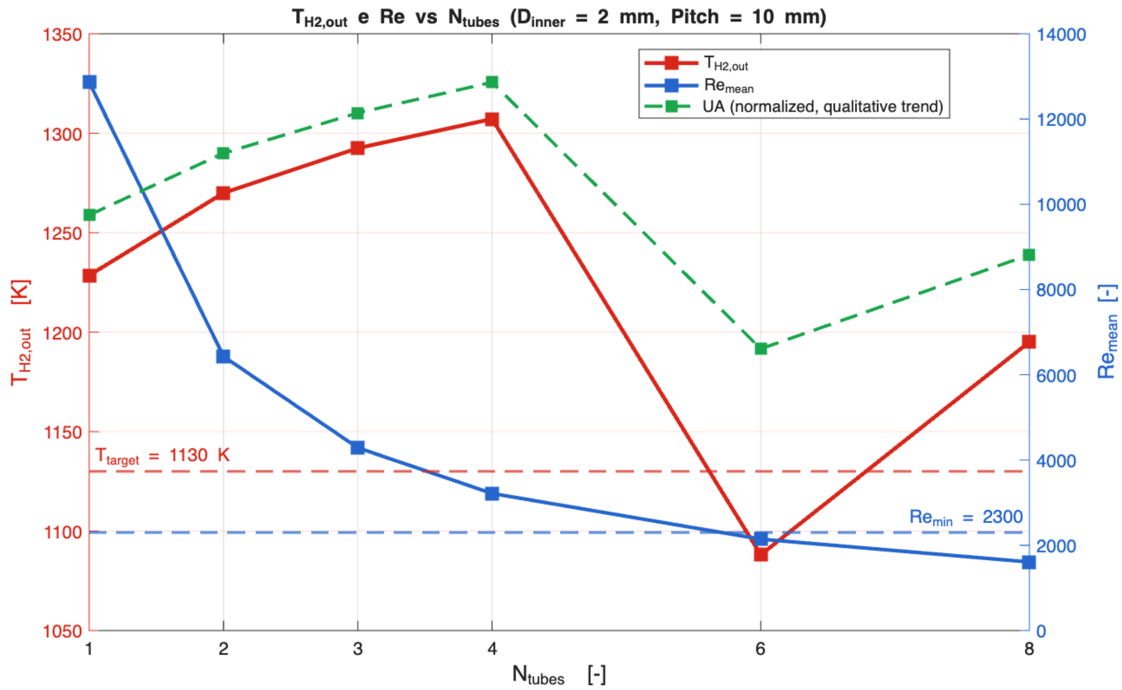

Figure 3.6: Effect of N_{tubes} on $T_{out,pr}$, Re_{mean} and UA for a fixed geometry

Finally, Figure 3.7 shows the pressure losses. As expected from Equation 3.5, increasing N_{tubes} or D_{inner} reduces the pressure drop because the total flow area increases and the average flow velocity decreases. The dashed line highlights the pressure-drop constraint adopted in this work, which is discussed in Section 3.4.2.

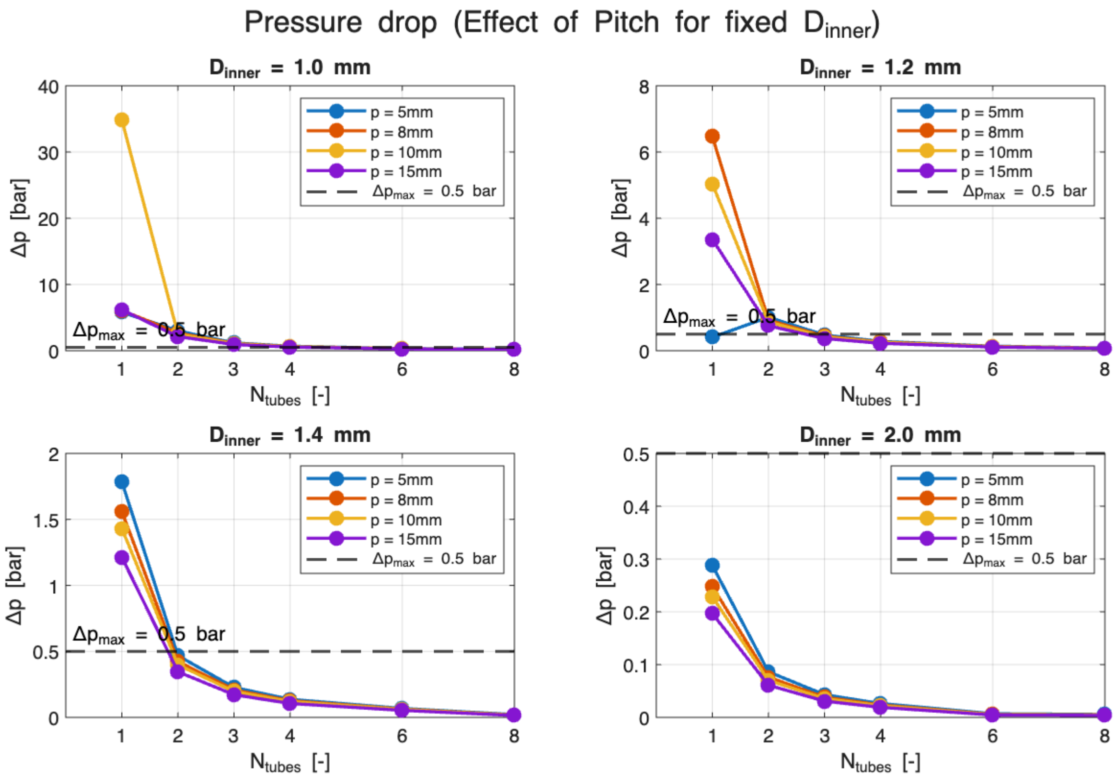

Figure 3.7: Pressure drop trends as a function of the N_{tubes} for different D_{inner} and p

3.4.2 Design constraints and UA Filtering

Geometric Constraints

Not all combinations of N_{tubes}, p, and D_{inner} produce feasible HEX geometries. The generated configurations were first screened through a preliminary geometric feasibility check.

This constraint prevents overlap between adjacent helical channels and ensures a minimum spacing between the channels. For a selected number of channels N_{tubes} and an inner channel diameter D_{inner}, the helical pitch p must satisfy:

$$p \geq N_{tubes} \cdot D_{inner} \tag{3.19}$$

In addition, a minimum axial margin of 0.4 mm was introduced between adjacent helical channels to avoid unrealistically compact geometries.

Configurations that did not satisfy the geometric feasibility check were excluded from further analysis, reducing the initial design space from 96 to 66 feasible configurations.

Thermal and Hydraulic Constraints

Additional thermal and hydraulic requirements were introduced to identify configurations with acceptable performance.

The outlet propellant temperature was required to satisfy

$$T_{out,pr} \geq 1130\ K \tag{3.20}$$

This represents the minimum thermal requirement of the propulsion system.

In addition, the pressure drop across the HEX was limited to 10% of the nominal inlet pressure to reduce hydraulic losses:

$$\Delta p \leq 0.5 \text{ bar} \tag{3.21}$$

Finally, a minimum mean Reynolds number of

$$Re_{mean} \geq 2300 \tag{3.22}$$

was imposed during the preliminary design exploration. Here, Re_{mean} refers to the Reynolds number defined in Eq. 3.4, which is estimated using average flow properties and constant propellant properties. For this reason, it was not used to strictly classify the flow regime. Instead, this threshold was selected to exclude configurations characterized by very low flow velocities and convective heat transfer without unnecessarily restricting the design space.

The adopted constraints are summarized in Table 3.5.

Among the 66 geometrically feasible configurations, 63 satisfied the outlet temperature requirement, 40 satisfied the pressure-drop constraint, and 64 satisfied the Reynolds-number constraint. When all constraints were applied simultaneously, 37 feasible configurations remained.

Constraint	Value	Motivation
Outlet temperature	$T_{out,pr} \geq 1130$ K	Propulsion requirement
Pressure drop	$\Delta p \leq 0.5$ bar	Acceptable hydraulic losses
Reynolds number	$Re \geq 2300$	Enhanced heat transfer

Table 3.5: Thermal and hydraulic constraints adopted during the preliminary design exploration

UA Filtering

An additional filter was then introduced based on the overall heat transfer conductance of the HEX, expressed through the parameter UA. As UA increases, the outlet propellant temperature approaches the wall temperature asymptotically. Beyond a certain value, further increases in UA produce only small temperature gains, while requiring larger heat transfer surfaces and leading to higher pressure losses.

To identify this region of limited thermal benefits, the $T_{out,pr}$ was plotted against UA for all feasible configurations (Figure 3.8).

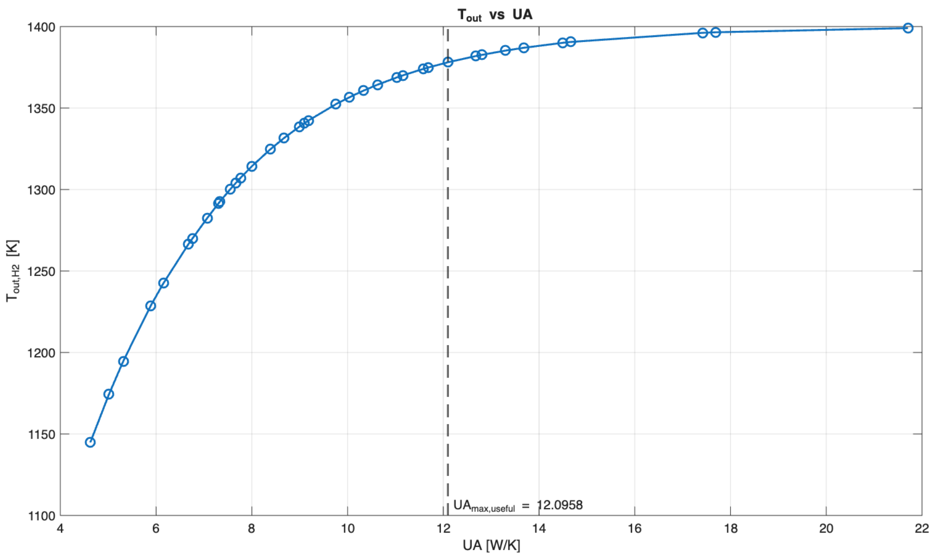

Figure 3.8: Outlet propellant temperature as a function of the overall heat transfer conductance for the feasible configurations

The configurations were first sorted according to increasing UA, and the local discrete slope

$$\frac{dT_{out}}{dUA} \tag{3.23}$$

was evaluated between consecutive points.

The beginning of the plateau region was identified when the local slope became lower than 10% of the maximum observed slope:

$$\frac{dT_{out}}{dUA} < 0.1 \left(\frac{dT_{out}}{dUA} \right)_{max} . \tag{3.24}$$

The corresponding slope values are reported in Figure 3.9.

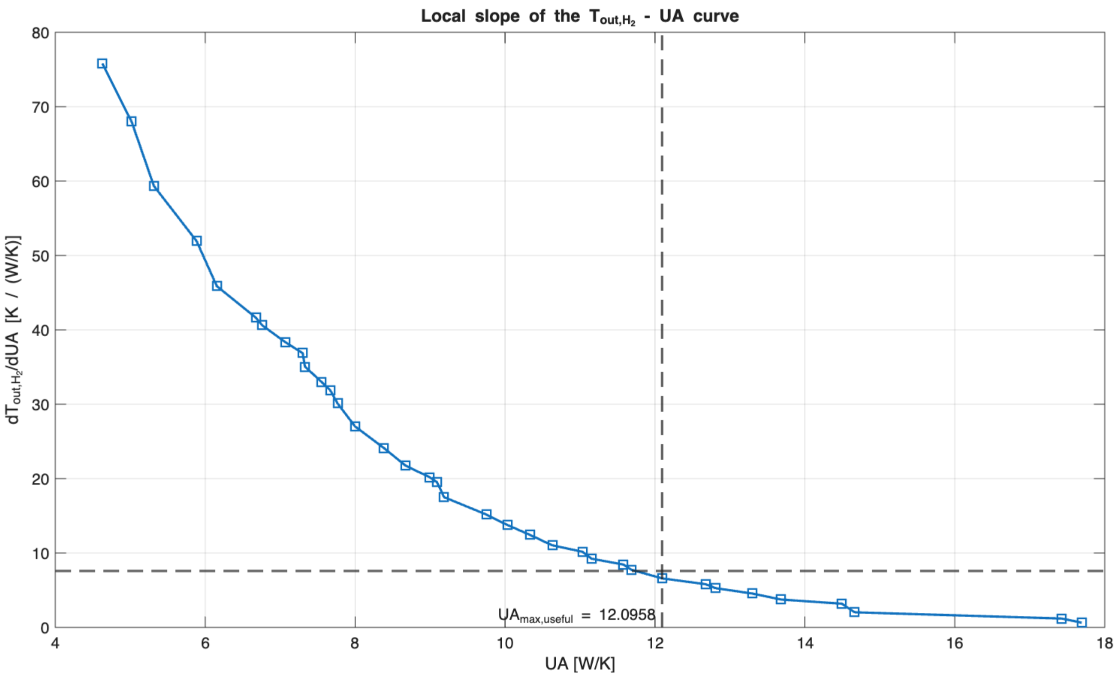

Figure 3.9: Local slope of the $T_{out,pr}$–UA curve used to identify the plateau region

This procedure led to a useful heat-transfer threshold of

$$UA_{max,useful} = 12.096\ W/K. \tag{3.25}$$

Configurations with larger UA values were excluded from the following analysis.

After applying the UA filter, 28 configurations remained for the trade-off analysis.

3.4.3 Pareto Analysis

The remaining feasible configurations were analysed using a two-objective Pareto approach.

The objective was to identify configurations capable of maximizing the overall heat transfer conductance, UA, while simultaneously minimizing hydraulic losses, Δp. Following a common practice in multi-objective optimization studies [22],[23], both objectives were formulated as minimization problems. Therefore, the thermal objective was expressed as $-UA$, while the pressure drop was directly minimized.

A configuration was considered Pareto-optimal when no other configuration simultaneously provided a lower value of $-UA$ and a lower pressure drop.

The resulting Pareto front contained seven non-dominated configurations out of the 28 feasible solutions (Figure 3.10).

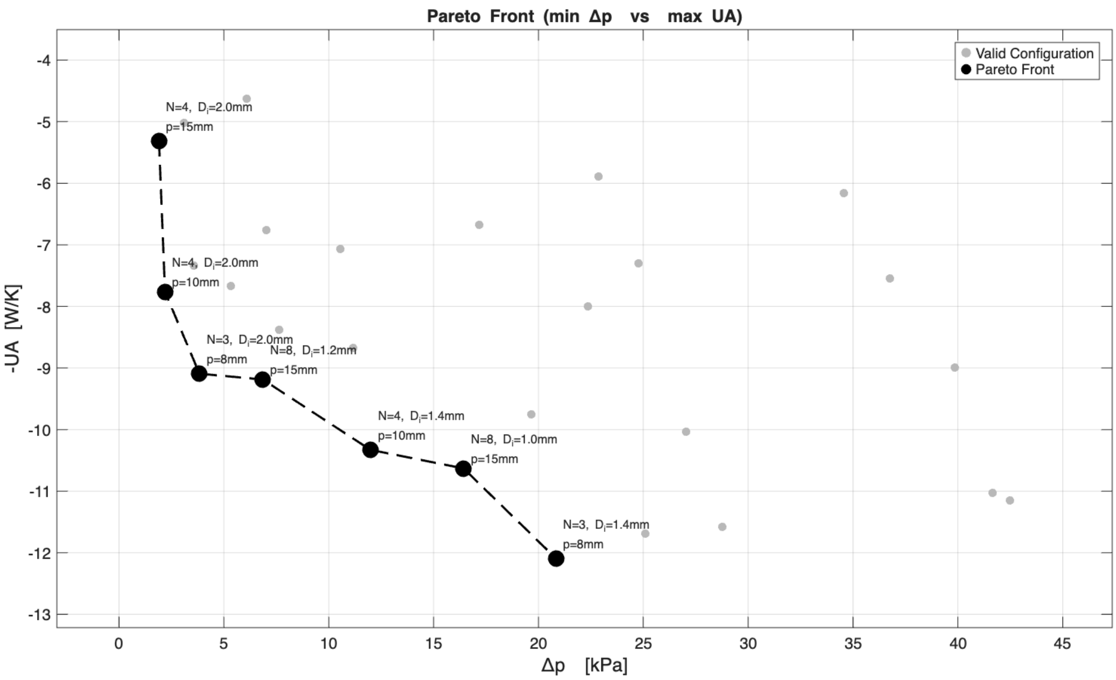

Figure 3.10: Pareto front

The Pareto analysis highlighted the existence of different design strategies characterized by trade-offs between thermal performance, compactness and hydraulic losses.

N_{tubes}	p **[mm]**	D_{inner} **[mm]**	**UA [W/K]**	Δp **[Pa]**
4	15.00	2.000	5.315	1904
4	10.00	2.000	7.766	2192
3	8.00	2.000	9.093	3834
8	15.00	1.200	9.187	6855
4	10.00	1.400	10.330	11996
8	15.00	1.000	10.630	16423
3	8.00	1.400	12.096	20846

Table 3.6: Pareto front configurations

3.4.4 Local Design Space Refinement

The initial design exploration identified the most promising region of the design space. Based on the Pareto-optimal configurations identified in Section 3.4.3, a second exploration was performed using a refined set of design variables.

Figure 3.11 shows the design variables associated with the Pareto-optimal configurations. They were used to define the refined design space adopted in the second exploration.

Note that the $UA_{max,useful}$ threshold defined in Section 3.4.2 was not applied in this refined exploration.

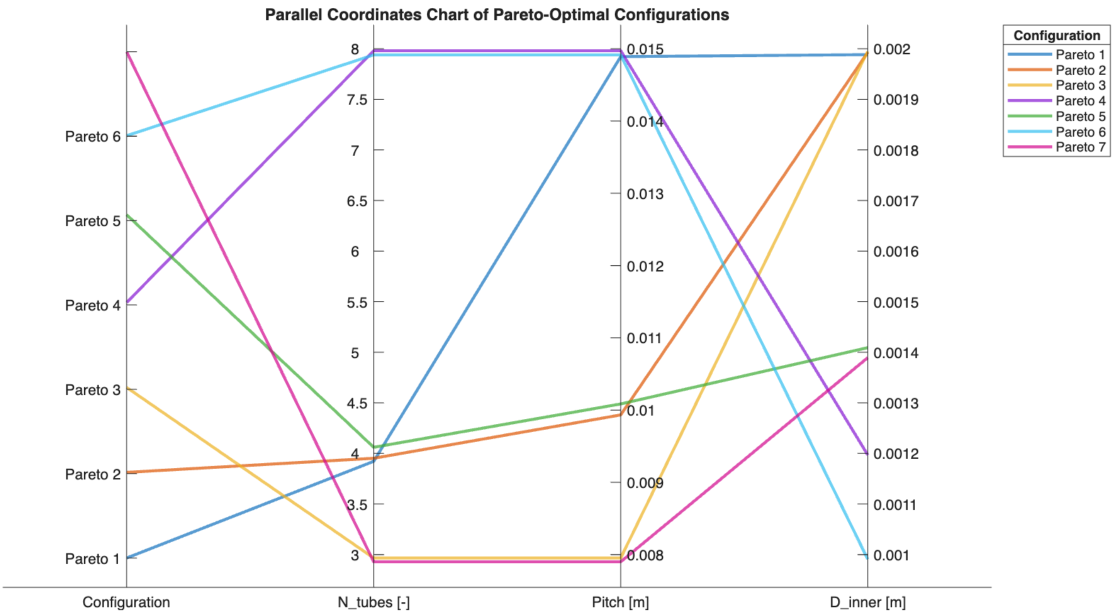

Figure 3.11: Geometric characteristics of the Pareto-optimal configurations identified during the initial design exploration

The ranges adopted for the refined exploration are summarized in Table 3.7.

Parameter	**Initial Range**	**Refined Range**
N_{tubes} [-]	1, 2, 3, 4, 6, 8	3, 4
p [mm]	5, 8, 10, 15	8 : 0.5 : 10
D_{inner} [mm]	1, 1.2, 1.4, 2	1.4 : 0.1 : 2

Table 3.7: Comparison between the initial and refined design spaces

The refinement increased the local resolution of the design space around the Pareto region, producing a larger number of feasible configurations. Figure 3.12 shows the resulting Pareto front.

Table 3.8 shows the configurations identified in the second Pareto front.

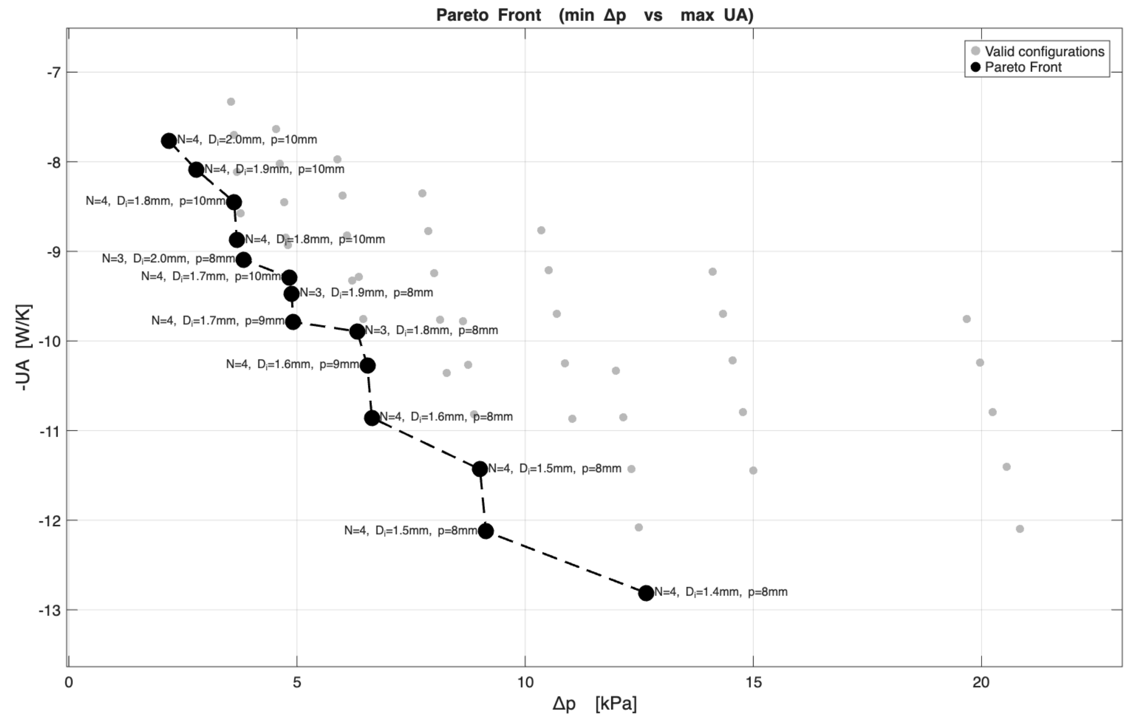

Figure 3.12: Pareto front obtained from the refined design space exploration

N_{tubes}	p **[mm]**	D_{inner} **[mm]**	**UA [W/K]**	Δp **[Pa]**
4	10.00	2.000	7.766	2192
4	10.00	1.900	8.091	2800
4	10.00	1.800	8.449	3623
4	9.50	1.800	8.875	3683
3	8.00	2.000	9.093	3834
4	9.50	1.700	9.290	4833
3	8.00	1.900	9.474	4889
4	9.00	1.700	9.786	4909
3	8.00	1.800	9.893	6317
4	9.00	1.600	10.273	6542
4	8.50	1.600	10.856	6641
4	8.50	1.500	11.432	9010
4	8.00	1.500	12.124	9140
4	8.00	1.400	12.812	12660

Table 3.8: Configurations identified in the refined design space exploration

3.4.5 Identification of Design Families

The refined exploration revealed the three main families of Pareto-relevant configurations.

The first family consists of conservative four-channel configurations characterized by large inner diameters, low pressure losses and moderate thermal performance.

The second family consists of three-channel configurations that provide a compromise between thermal performance, Reynolds number and geometrical simplicity.

The third family consists of compact four-channel configurations characterized by higher heat-transfer conductance and outlet temperatures, but also larger pressure losses.

These families guided the final CFD configuration selection.

3.4.6 Selection of CFD Configurations

Three representative configurations were selected for CFD investigation (Table 3.9).

The aim of the selection was not to identify a single optimal solution, but rather to investigate different regions of the design space and understand how the thermal-hydraulic behaviour changes across different design choices.

Configuration	N_{tubes}	$p[mm]$	$D_{inner}[mm]$
C1	4	10	2
C2	3	8	2
C3	4	8	1.5

Table 3.9: Selected CFD configurations

The selected configurations represent the basis of the CFD analyses presented in Chapter 4.

3.5 Sensitivity to Convective Heat Transfer Correlations

The preliminary thermal sizing of the helical-tube HEX is based on the Dittus-Boelter correlation, which is used to estimate the Nusselt number and the convective heat transfer coefficient. This correlation is commonly adopted in preliminary design studies because of its simplicity and its applicability to turbulent flow in circular tubes [24], [25].

However, the operating conditions of a hydrogen-fuelled STT involve high temperatures and large wall-to-bulk temperature differences. Under these conditions, the predicted heat transfer may depend on the selected Nusselt correlation. For this reason, a sensitivity analysis was carried out to assess how the choice of correlation influences the results obtained from the preliminary model.

In addition to the baseline Dittus-Boelter formulation, three alternative correlations were applied to the entire design-space exploration: the Gnielinski correlation, the McCarthy & Wolf correlation, and the Westinghouse correlation. The Gnielinski correlation extends the applicability of the model over a wider range of Reynolds numbers by including the effect of the friction factor [26]. The McCarthy & Wolf and Westinghouse correlations were originally developed for high-temperature hydrogen and helium flows and include a correction term based on the wall-to-bulk temperature ratio. The Westinghouse correlation also accounts for entrance-region effects [27].

Figure 3.13 compares the Nusselt numbers predicted by the different correlations as a function of the Reynolds number range.

All correlations predict the expected increase in Nusselt number with Reynolds number and show similar overall trends. The Dittus-Boelter and Gnielinski correlations generally provide higher Nusselt numbers, while the McCarthy & Wolf and Westinghouse formulations give more conservative predictions. These differences are associated with the temperature-ratio correction included in the hydrogen-specific correlations.

Although the predicted Nusselt numbers differ, the overall behaviour of the configurations remains consistent across the investigated design space. The sensitivity analysis therefore provides an indication of the uncertainty associated with the heat-transfer model and confirms that the main trends observed during the preliminary design exploration are not significantly affected by the selected correlation.

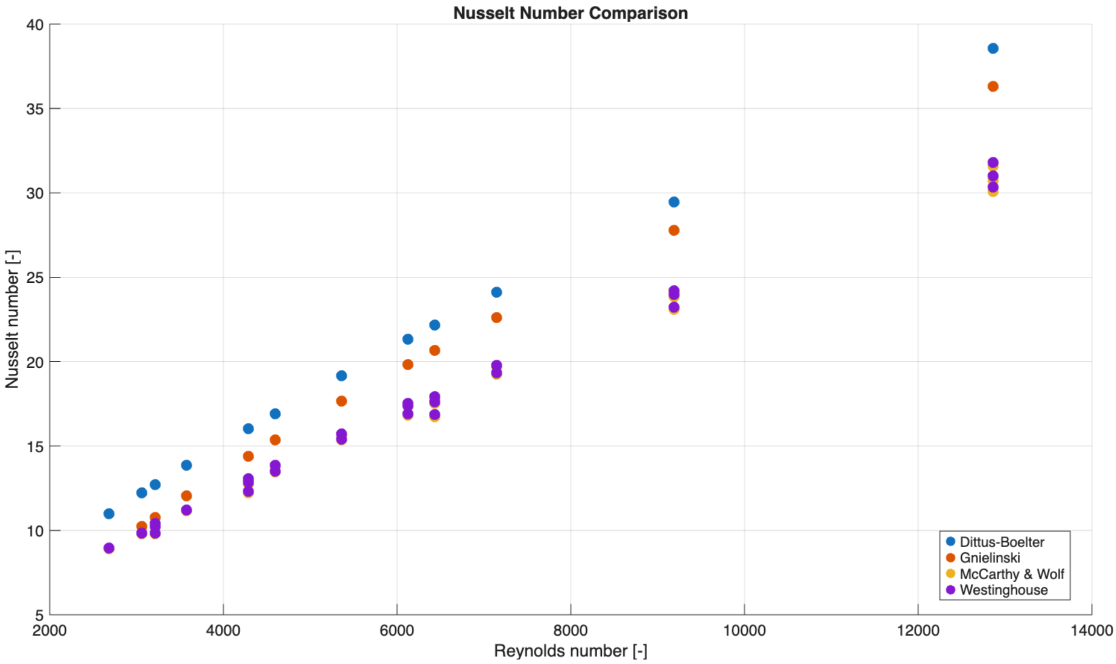

Figure 3.13: Comparison of predicted Nusselt numbers vs Reynolds number for the convective heat transfer correlations

Chapter 4

CFD Methodology

Figure 4.1 summarizes the main steps of the CFD workflow adopted in the present study to simulate the three configurations selected in Section 3.4.6, from geometry preparation to post-processing.

4.1 Computational Domain and Geometric Model

The CFD analysis was performed on a three-dimensional model of the receiver - absorber HEX selected during the preliminary design phase. The geometry consists of a cylindrical body containing multiple helical flow channels through which gaseous hydrogen flows. Because of the absence of geometric symmetry in the helical channel arrangement, the complete 360° geometry was considered in all simulations.

The CAD model was created in Autodesk Fusion 360 and imported into ANSYS Workbench for geometry preparation. Two computational regions were identified: a solid domain representing the aluminium HEX structure and a fluid domain representing the hydrogen flow (Figure 4.2).

Generally, TES and HEX are treated as distinct components and may be manufactured from different materials. In the present work, an integrated RAC architecture is considered, where both functionalities could potentially be combined into a single additively manufactured component. However, the identification of a

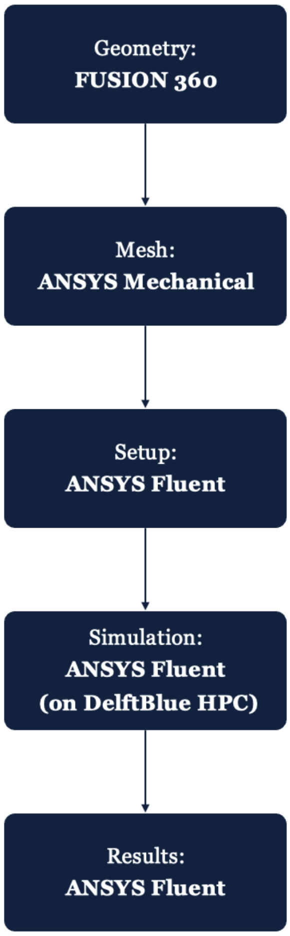

Figure 4.1: CFD workflow

suitable material is beyond the scope of the present study.

Graphite was not considered representative of a realistic HEX structure because of its limited compatibility with hydrogen, manufacturing constraints (challenges associated with AM), and low thermal conductivity compared to metallic materials. Therefore, although graphite was used in the preliminary MATLAB framework (Section 3.3.1), aluminium was selected for the CFD simulations to better represent the HEX structure.

Furthermore, since the CFD analysis is performed under steady-state conditions with a constant wall temperature, the influence of the solid material properties on the predicted fluid thermal-hydraulic behaviour is expected to be negligible.

Both regions were included in the computational domain in order to model the heat transfer between the aluminium structure and the hydrogen flow through a CHT approach [28].

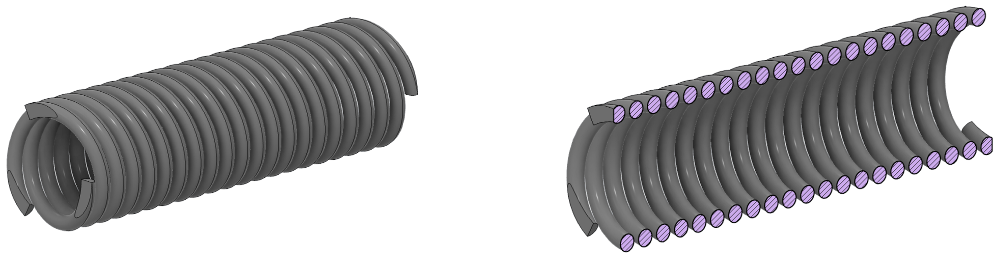

(a) Fluid domain

(b) Fluid domain section

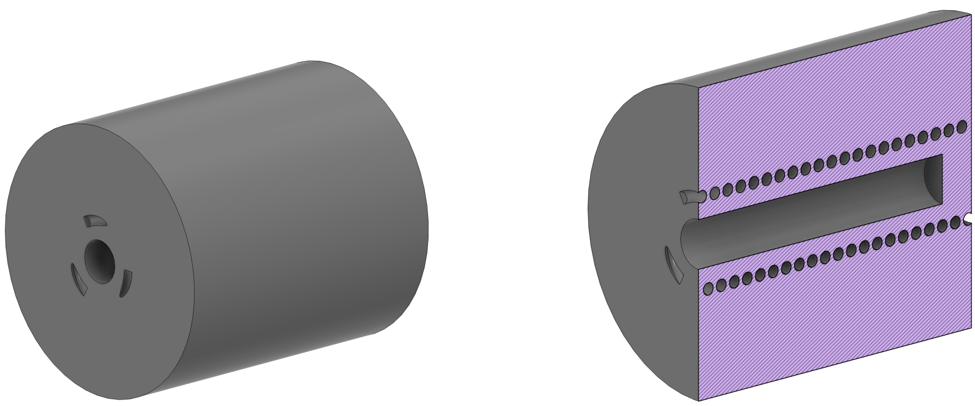

(c) Solid wall

(d) Solid wall section

Figure 4.2: Fluid and solid computational domains generated in Fusion 360

Before meshing, a set of Named Selections was defined to facilitate the assignment of boundary conditions and the coupling between the two domains. These include the inlet (Fig. 4.3a) and outlet (Fig. 4.3b) surfaces of the hydrogen flow, the cavity surface (Fig. 4.3c) subjected to the imposed thermal load, and the solid-fluid interfaces used to transfer heat between the solid and the fluid domain (Fig. 4.3d and Fig. 4.3e).

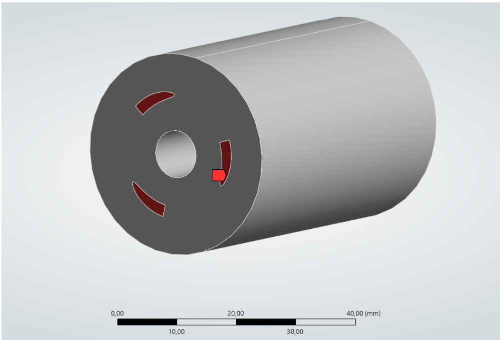

(a) Inlet

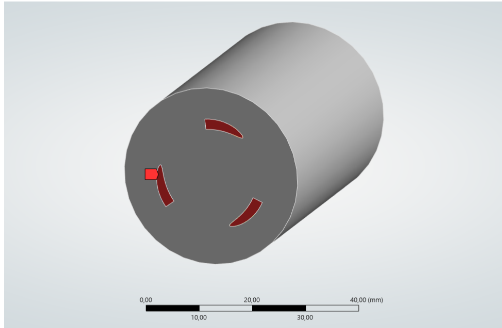

(b) Outlet

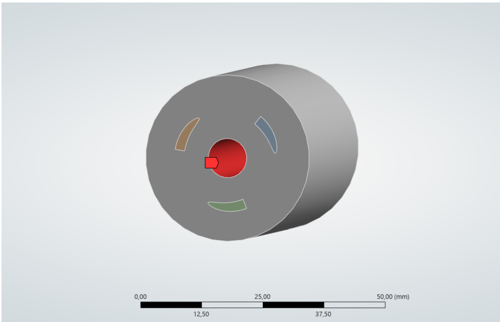

(c) Cavity

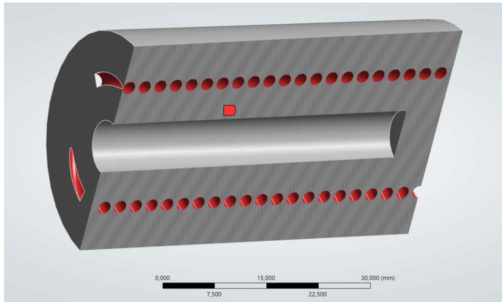

(d) Wall–fluid interface

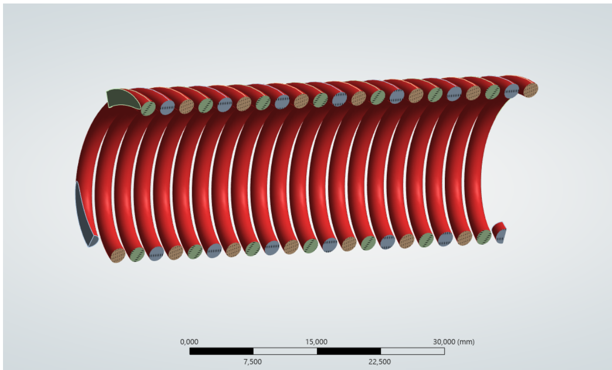

(e) Fluid–wall interface

Figure 4.3: Named selections defined in ANSYS Mechanical

4.2 Turbulence Modeling

The flow inside the helical channels is characterized by effects induced by the curvature and secondary flow structures, which can influence both pressure losses and heat transfer. To model these phenomena, a Reynolds-Averaged Navier-Stokes

(RANS) approach was adopted.

The Realizable k-ε model was selected as the baseline turbulence model for the present study. Compared with the Standard k-ε formulation, it generally provides improved predictions for flows characterized by rotation, curvature, and separation, making it suitable for the helical channel geometry investigated in this work [29]. For this reason, all reference CFD simulations were initially performed using the Realizable k-ε model.

In addition, the Standard k–ε and Shear Stress Transport (SST) k–ω models were used to assess the sensitivity of the numerical results. The Standard k-ε model was considered because of its widespread use and computational robustness, while the SST k-ω model was included due to its accurate near-wall treatment and its frequent application in aerospace and turbomachinery applications where the prediction of boundary-layer behaviour is particularly important [29], [30]. The influence of the selected turbulence model on the predicted thermal and hydraulic performance is discussed in Section 5.3.

4.3 Near-Wall Treatment and Boundary-Layer Resolution

Since the highest temperature gradients are close to the solid-fluid interface, the prediction of heat transfer and pressure losses is influenced by the near-wall flow behaviour. For this reason, this region must be accurately resolved.

In turbulence modelling, the resolution of the first layer of mesh cells near the wall is commonly evaluated using the dimensionless parameter y^+. It represents the distance of the first computational node from the wall:

$$y^+ = \frac{y \cdot u_\tau}{\nu} \tag{4.1}$$

where:

- y is the normal distance from the wall to the first computational grid point
- u_τ is the friction velocity, calculated using $u_\tau = \sqrt{\frac{\tau_w}{\rho}}$, where τ_w is the wall shear stress

- ν is the kinematic viscosity of the fluid

The turbulent boundary layer is divided into three regions [29], [31]:

- Viscous sublayer ($y^+ < 5$). It is the region closest to the wall, where viscosity dominates and the velocity profile is approximately linear.
- Buffer layer ($5 < y^+ < 30$). It represents the transition between viscous and turbulent flow.
- Log layer ($y^+ > 30$). It is the region where the flow is dominated by turbulence and the velocity profile follows the logarithmic law:

$$u^+ = \frac{1}{k} \cdot ln(y^+) + C^+ \tag{4.2}$$

where u^+ is the dimensionless velocity, $k \approx 0.41$ is the von Kármán constant and C^+ is an empirical constant.

The simulations were performed using the Realizable $k - \varepsilon$ turbulence model with Enhanced Wall Treatment (EWT). This approach was selected because it provides a more accurate results for different near-wall mesh resolutions, and it improves the treatment of the buffer layer, where Standard Wall Functions are less accurate.

Although EWT can be used with higher y^+ values, the prediction is more accurate when the first computational node is inside the viscous sublayer. For this reason, the first cell height was selected to achieve a target value of $y^+ \approx 1$, through the use of inflation layers along the fluid-solid interfaces [30].

The quality of the near-wall mesh was then assessed through a mesh refinement study, as discussed in Chapter 5.

4.4 Spatial Discretization and Mesh

The computational domain was discretized using an unstructured mesh generated in ANSYS Mechanical. Due to the complexity of the helical flow channels, an unstructured approach was selected to preserve the geometric features of the model while maintaining meshing flexibility. For the baseline mesh, a global element size (Figure 4.4) was adopted for the solid domain and for the fluid domain.

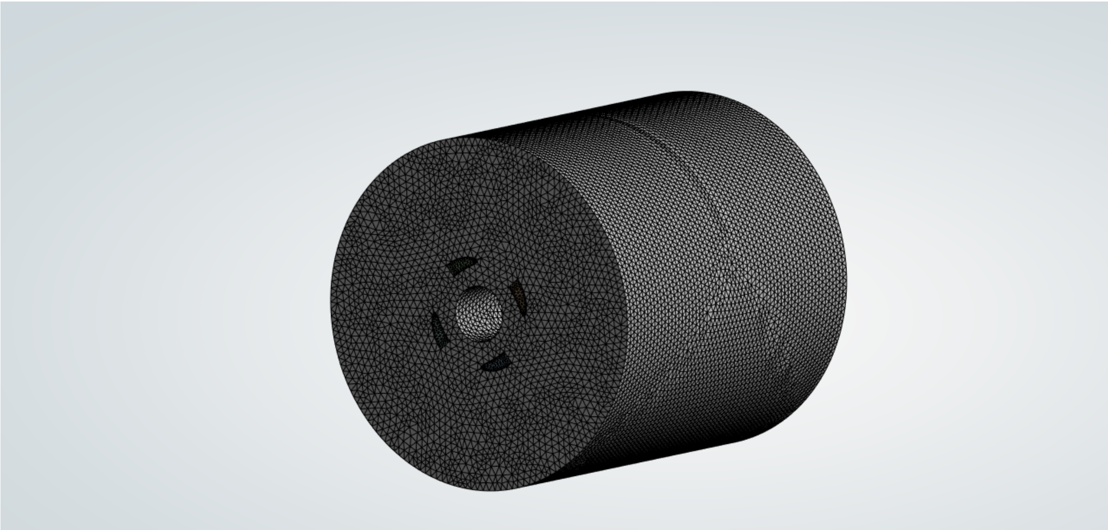

Figure 4.4: Global baseline mesh

Additional refinement was introduced near the solid–fluid interface, where the highest velocity and temperature gradients are expected. In these regions, the maximum element size was reduced (Figure 4.5), and a local edge sizing (Figure 4.6) was applied in areas with strong curvature. These local sizing controls were included in both mesh configurations considered in the present work.

A second mesh configuration was generated by introducing three inflation layers (Figure 4.7) along the channel walls to improve the resolution of the boundary layer. The inflation layers were defined setting a value for the first layer height and the growth rate. Their purpose was to improve the resolution of the near-wall region and satisfy the requirements of the turbulence models adopted in the study [29].

Two mesh configurations were therefore considered during the CFD campaign: a baseline mesh including global and local sizing controls, and a refined mesh obtained by adding inflation layers to the baseline one. The Realizable k-ε model was simulated on both meshes to assess the influence of near-wall refinement on the resulting thermal and hydraulic performance. The Standard k-ε and SST k-ω models were instead assessed only on the refined mesh, because it provides a near-wall resolution more suitable the SST formulation [29].

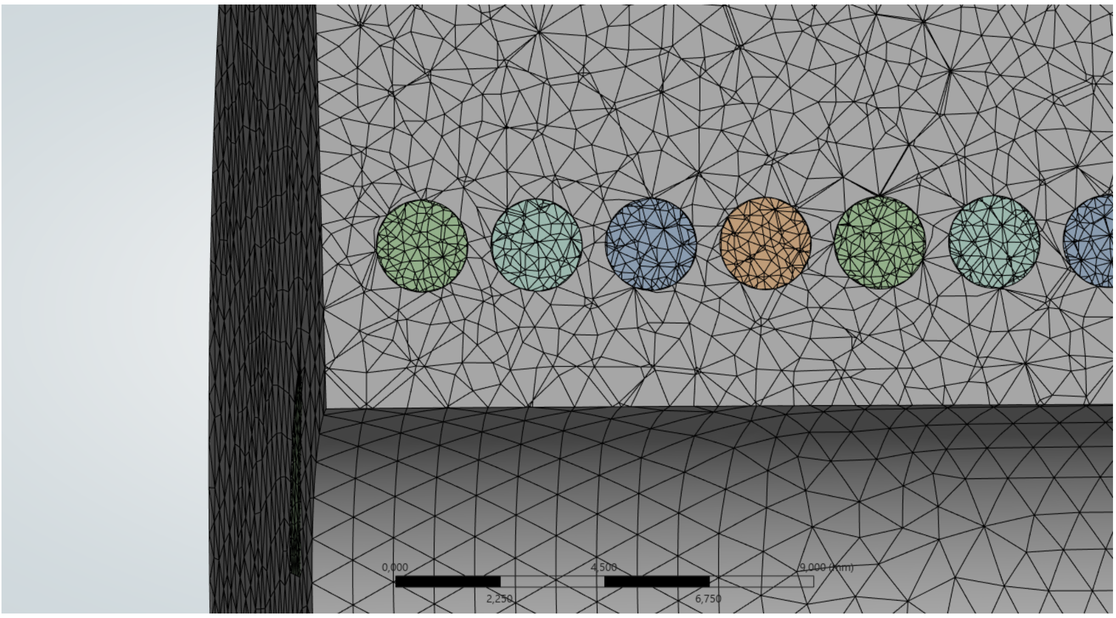

Figure 4.5: Face sazing (Interface fluid-wall)

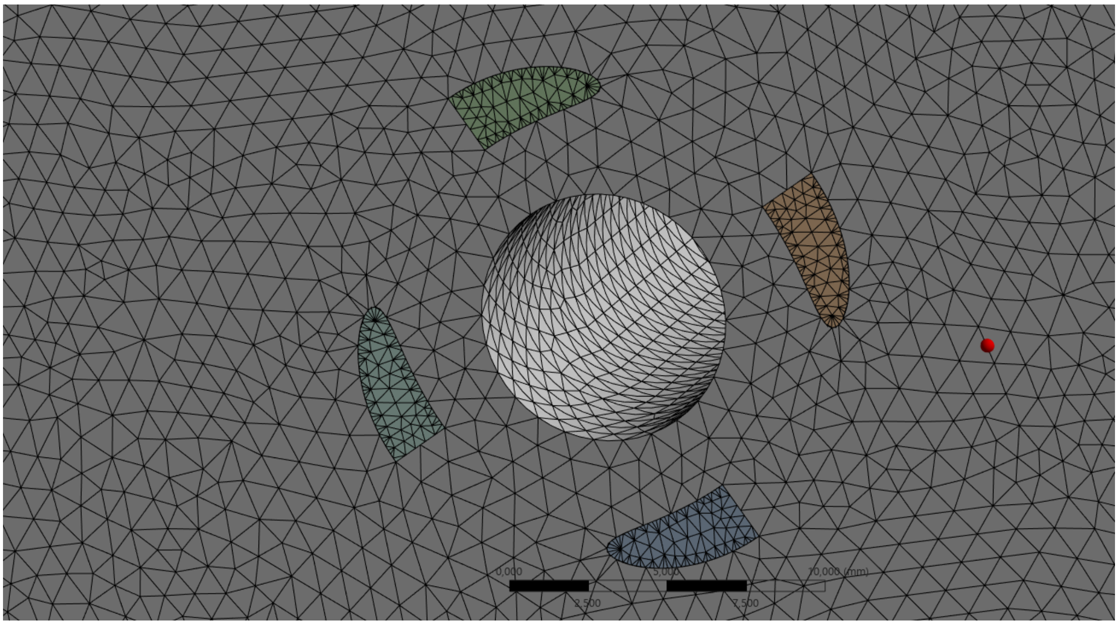

Figure 4.6: Edge sizing

The figures show the mesh generation procedure for a representative configuration (4 channels, $D_{inner} = 2$ mm, $p = 10$ mm). The same meshing approach was applied

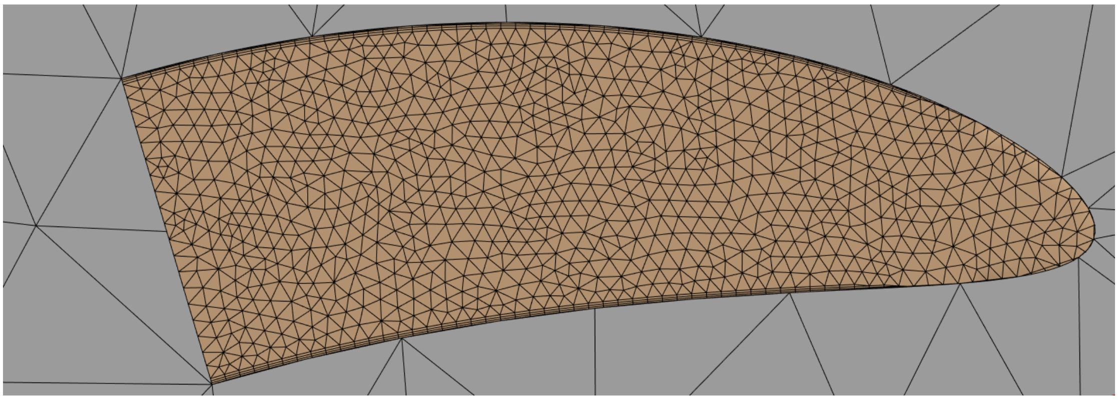

Figure 4.7: Inflation layers

to all CFD geometries, with the introduction of small adjustments to the sizing parameters when required by the specific geometry. A summary of the mesh settings adopted for each configuration is provided in Table 4.1.

Parameter	**Config. 1**	**Config. 2**	**Config. 3**
Solid sizing [mm]	1.0	0.5	1.0
Fluid sizing [mm]	0.40	0.40	0.30
Interface sizing [mm]	0.30	0.30	0.25
Edge sizing [mm]	0.15	0.15	0.05
Inflation layers [-]	3	3	3
First layer height [mm]	0.01	0.01	0.008
Growth rate [-]	1.2	1.2	1.2

Table 4.1: Meshing parameters adopted for the selected CFD configurations

4.5 Boundary Conditions

The CFD simulations were performed using boundary conditions representative of the operating conditions considered during the preliminary design phase. The adopted values are summarized in Table 4.2.

A Mass Flow Inlet boundary condition was applied at the channel inlet. The total hydrogen mass flow rate was fixed at 0.177 g/s and equally distributed among the helical channels (three or four channels, depending on the specific geometric configuration). The propellant enters the HEX at a temperature of 300 K and an inlet pressure of 500 kPa.

A Pressure Outlet boundary condition of 101325 Pa was applied at the channel outlet. Although the final propulsion system is intended to operate in space, atmospheric pressure was selected in the present work to represent ground-based testing conditions. This choice provides a conservative reference case before future vacuum tests.

A fixed temperature of 1400 K was imposed on the cavity surface to represent the thermal input provided by the solar concentrator. This value was assumed during the preliminary design phase and used throughout the CFD analysis.

The solid and fluid domains were thermally connected through the interfaces, allowing heat transfer between the two regions.

Zone	**Boundary Type**	**Value**
Inlet	Mass Flow Inlet	$\dot{m}_p = 0.177\,\mathrm{g\,s^{-1}}$ (total)
		$T_{in} = 300\,\mathrm{K}$
		$p_{in} = 500\,000\,\mathrm{Pa}$
Outlet	Pressure Outlet	$p_{out} = 101\,325\,\mathrm{Pa}$
Cavity	Fixed Temperature	$T_{wall} = 1400\,\mathrm{K}$

Table 4.2: Boundary conditions applied in the CFD simulations

4.6 Numerical Setup and HPC

All simulations were performed using ANSYS Fluent 2024 R2. A pressure-based coupled solver was adopted and the default solution methods available in ANSYS Fluent were used. Second-order upwind discretization schemes were used for pressure, density, momentum, and energy, to reduce numerical diffusion and improve the prediction of flow and thermal gradients, which are particularly important in turbulent heat-transfer applications, as recommended in the Fluent documentation. For the turbulence quantities (turbulent kinetic energy and dissipation rate), a first-order upwind discretization was adopted. The Fluent guidelines recommend a conservative approach for these variables, since the turbulence equations are strongly coupled with the mean flow equations, and can introduce convergence difficulties with higher-order schemes. The maximum number of iterations was set to 10,000 for each simulation. The convergence criterion for the energy equation was set to 10^{-6}, while a value of 10^{-3} was adopted for continuity, momentum, turbulent kinetic energy, and turbulent dissipation rate. The settings are reported in Table 4.3 [29], [32].

Setting	**Value**
Solver	Pressure-Based Coupled
Pressure	Second Order
Density	Second Order Upwind
Momentum	Second Order Upwind
Energy	Second Order Upwind
Turbulent Kinetic Energy	First Order Upwind
Turbulent Dissipation Rate	First Order Upwind
Energy residual	10^{-6}
Other residuals	10^{-3}
Maximum iterations	10 000

Table 4.3: Solution methods adopted in the CFD simulations

Due to the size of the computational meshes and the computational cost associated with the 3D simulations, all analyses were performed on the DelftBlue High-Performance Computing (HPC) cluster at TU Delft. The standard job array was parallelized using a Message Passing Interface (MPI) architecture, allocating 56 processes (ntasks=56) with one Central Processing Unit (CPU) per task and 3 GB of memory per node. A standard wall-clock time limit of one hour was initially assigned to each job and increased when required for the most demanding cases.

Chapter 5

Results and CFD Assessment

The results presented in this chapter provide the basis for assessing the third research question defined in Chapter 1.

5.1 Comparison between MATLAB predictions and CFD Results

The three configurations selected in Section 3.4.6 were assessed through steady-state CHT CFD simulations.

5.1.1 Outlet Temperature

The comparison is first carried out in terms of hydrogen outlet temperature, reported in Table 5.1.

Config.	N_{tubes}	p **[mm]**	D_{inner} **[mm]**	$T_{\text{out,MATLAB}}[K]$	$T_{\text{out,CFD}}$ **[K]**
C1	4	10	2	1307	1349
C2	3	8	2	1341	1220
C3	4	8	1.5	1378	1283

Table 5.1: Comparison between MATLAB predictions and CFD results in terms of outlet temperature

The CFD results remain in the same temperature range predicted by the MATLAB model for all configurations. Configuration C1 shows the closest agreement, but all three configurations remain above the target value of 1130 K.

These results indicate that the preliminary model gives a reasonable prediction of the thermal behaviour of the selected configurations. The differences between MATLAB and CFD are expected, since the preliminary model uses a simplified one-dimensional approach, while the CFD simulation relies on the full three-dimensional temperature distribution along the helical channels.

5.1.2 Pressure Drop

The configurations were then compared in terms of pressure drop, as reported in Table 5.2.

Config.	N_{tubes}	p **[mm]**	D_{inner} **[mm]**	Δp_{MATLAB} **[Pa]**	Δp_{CFD} **[Pa]**
C1	4	10	2	2192	46876
C2	3	8	2	3834	83127
C3	4	8	1.5	9140	137969

Table 5.2: Comparison between MATLAB predictions and CFD results in terms of pressure drop

In this case, the CFD simulations predict significantly higher pressure losses than the MATLAB model for all configurations. The discrepancy cannot be attributed only to the assumptions of the near-1D model, especially because pressure losses are particularly sensitive to near-wall resolution and mesh refinement, as discussed in Section 5.4. The discrepancy is therefore related to a combination of the simplified hydraulic formulation adopted in the preliminary model and the numerical uncertainties of the CFD simulations. Nevertheless, both approaches predicted the same trend, with pressure losses increasing from Configuration C1 to C3.

Overall, the comparison highlights two different behaviours. The thermal performance predicted by the preliminary model is consistent with the CFD results, while the hydraulic performance shows larger discrepancies. The preliminary methodology can be considered a useful screening tool, while further verification is required for a quantitative assessment of the pressure losses.

5.2 Temperature and Pressure Fields

The temperature and pressure contours are presented to support the quantitative results discussed in the previous section and to visualise the flow evolution inside the helical channels.

Figure 5.1 shows the temperature field for Configuration C1. The largest temperature gradients are observed near the inlet, where the temperature difference between the wall and the hydrogen is the highest. The gradients then become progressively smaller, as the hydrogen flows through the channels and its temperature increases.

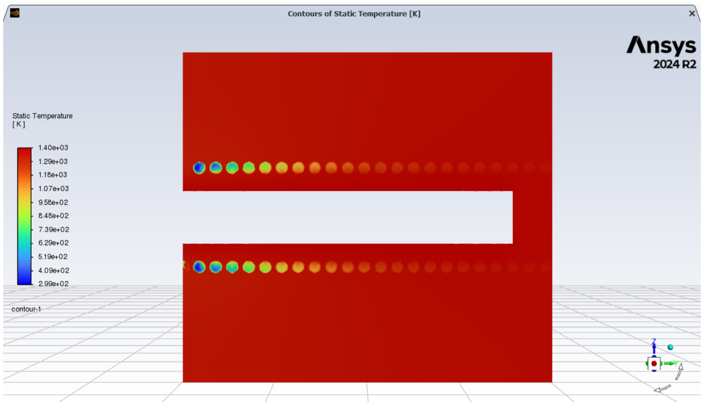

(a) Longitudinal section

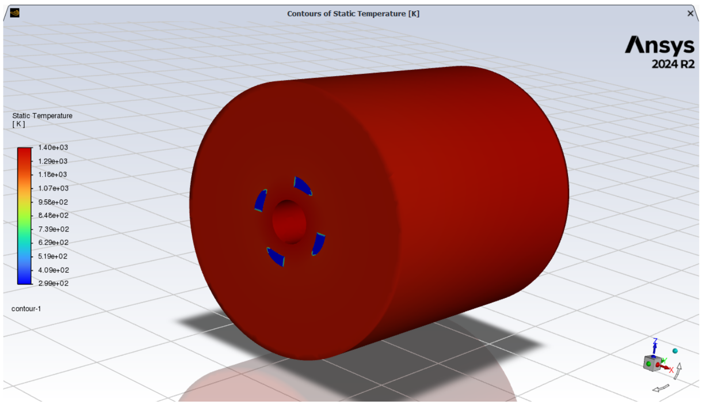

(b) Inlet view

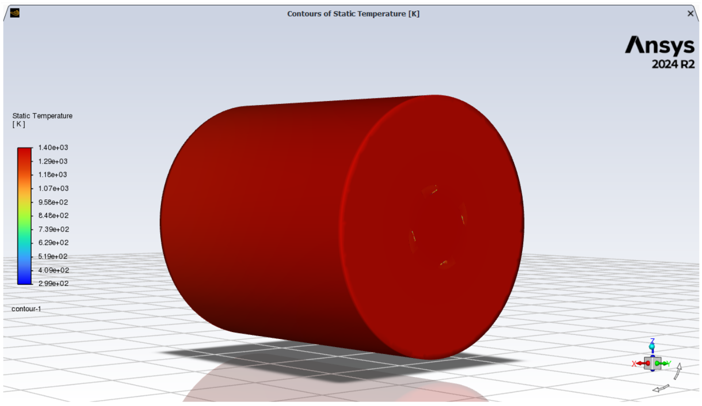

(c) Outlet view

Figure 5.1: Temperature contours for Configuration 1 obtained with the Realizable k–ε model and refined mesh

Figure 5.2 shows the corresponding pressure field. The pressure decreases smoothly along the helical path.

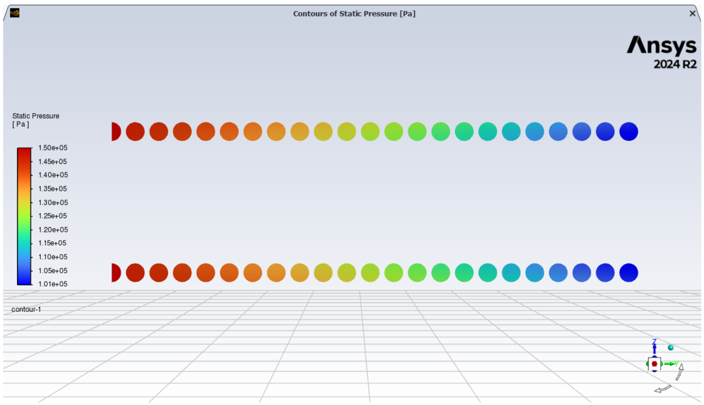

(a) Longitudinal section

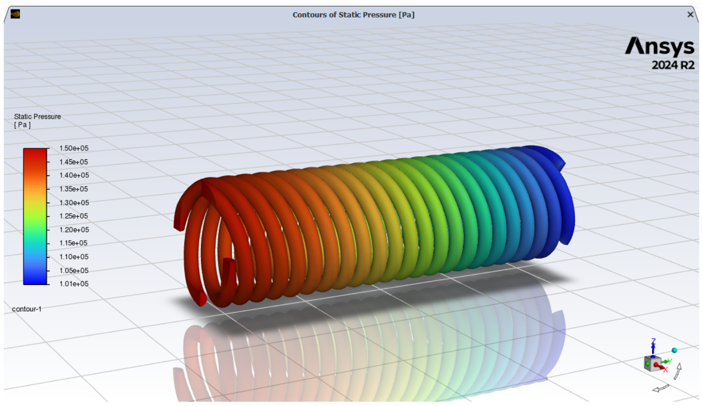

(b) Inlet view

Figure 5.2: Pressure contours for Configuration 1 obtained with the Realizable k–ε model and refined mesh

Figures 5.3 and 5.4 show the temperature and pressure fields for Configuration C2. The temperature contours confirm the same trend as C1, although the different number of channels and pitch lead to a different temperature distribution with a lower outlet temperature.

The pressure contours also show the same trend as C1, but with a higher overall pressure drop, consistent with the values reported in Table 5.2. This confirms the hydraulic trade-off already discussed during the preliminary design phase (Section 3.4.1): configurations that improve heat transfer through more compact geometries may lead to larger pressure losses.

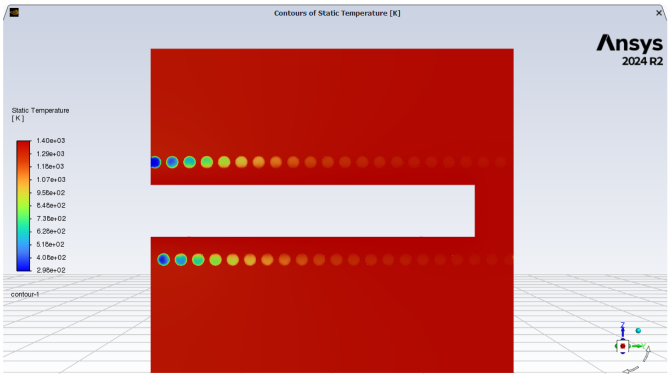

(a) Longitudinal section

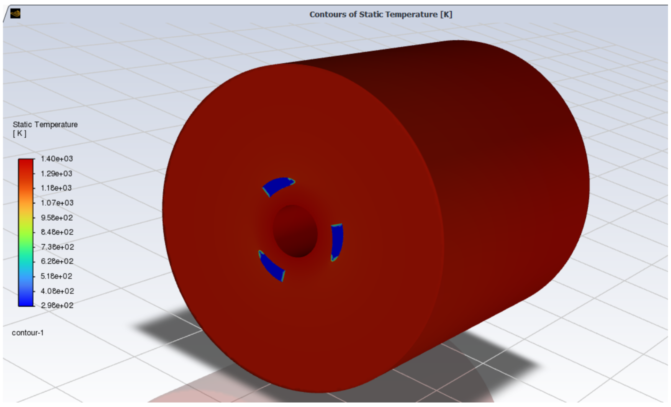

(b) Inlet view

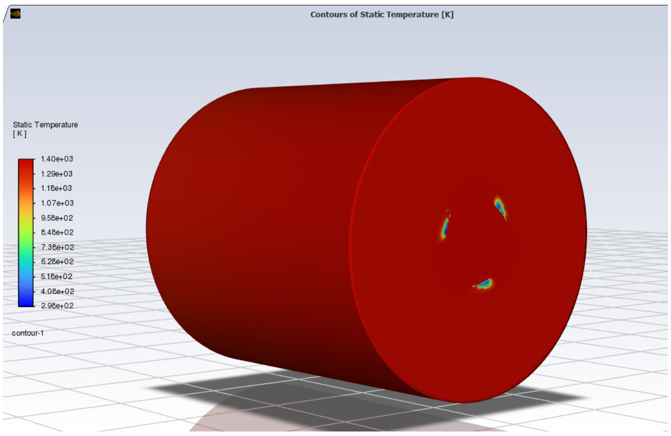

(c) Outlet view

Figure 5.3: Temperature contours for Configuration 2 obtained with the Realizable k–ε model and refined mesh

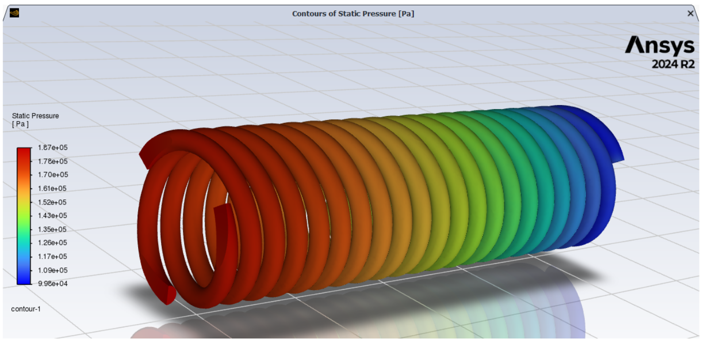

(a) Inlet view

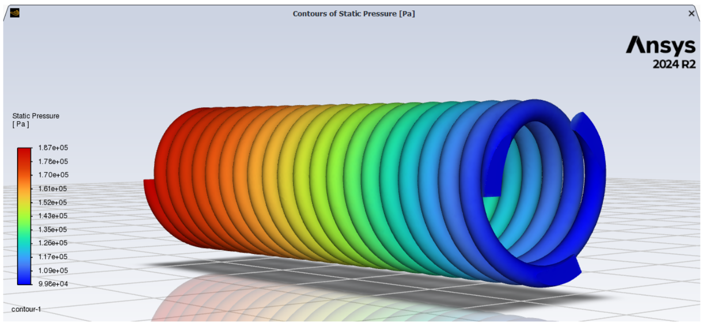

(b) Outlet view

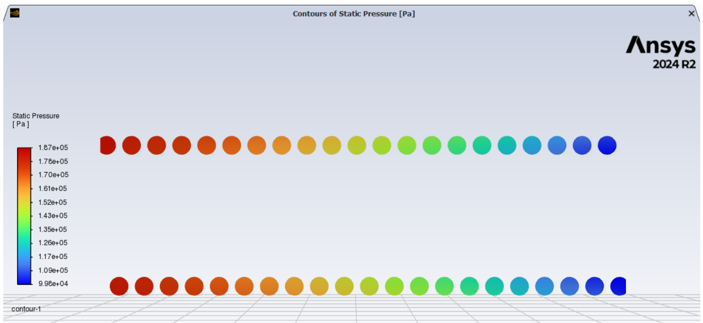

(c) Longitudinal section

Figure 5.4: Pressure contours for Configuration 2 obtained with the Realizable k-ε model and refined mesh

Overall, the contour plots are consistent with the outlet temperatures and pressure drops reported in the previous Section 5.1. The temperature fields show the progressive heating of the hydrogen along the helical channels, while the pressure fields show a continuous accumulation of hydraulic losses.

5.3 Turbulence Model Sensitivity

A turbulence model sensitivity analysis was performed on the refined mesh to evaluate the influence of the turbulence model choice on the CFD results. The Standard k-ε, Realizable k-ε, and SST k-ω models were used for the three selected configurations.

The results, reported in Tables 5.3, 5.4, and 5.5, show limited differences in outlet temperature and pressure drop among the different turbulence models. For Configuration C1, both quantities remain almost unchanged regardless of the selected model. Slightly larger differences are observed for Configurations C2 and C3, but the overall trends remain the same.

Turbulence Model	T_{out} **[K]**	Δp **[Pa]**
Standard k–ε	1349.28	46881
Realizable k–ε	1349.36	46876
SST k–ω	1349.28	46840

Table 5.3: CFD results obtained for Configuration 1 using different turbulence models with the same mesh

Turbulence Model	T_{out} **[K]**	Δp **[Pa]**
Standard k–ε	1280.47	83112
Realizable k–ε	1219.98	83127
SST k–ω	1308.81	78070

Table 5.4: CFD results obtained for Configuration 2 using different turbulence models with the same mesh

Turbulence Model	T_{out} **[K]**	Δp **[Pa]**
Standard k–ε	1284.54	137983
Realizable k–ε	1282.62	137969
SST k–ω	1308.27	137821

Table 5.5: CFD results obtained for Configuration 3 using different turbulence models with the same mesh

Overall, the CFD results are not strongly affected by the turbulence model choice. The Realizable $k-\varepsilon$ model was therefore selected as the baseline turbulence model of the study, remaining consistent with the approach adopted throughout the CFD analysis.

5.4 Mesh Independence Assessment

A mesh refinement study was performed to assess the influence of grid resolution on the CFD results and to verify the adequacy of the near-wall discretization adopted for the selected turbulence model.

Particular attention was given to the near-wall region, since the simulations were performed using the Realizable k-ε model with EWT, which requires sufficiently small y^+ values to accurately resolve the boundary layer.

The average y^+ values obtained with the base and refined meshes are reported in Table 5.6.

For all configurations, mesh refinement significantly reduced the average y^+ values, bringing them below unity.

The refinement improved the near-wall resolution and is consistent with the requirements of the EWT approach.

Configuration	N_{tubes}	p **[mm]**	D_{inner} **[mm]**	y^+_{avg} **base**	y^+_{avg} **refined**
C1	4	10	2.0	9.99	0.7046
C2	3	8	2.0	12.29	0.9011
C3	4	8	1.5	13.31	0.8708

Table 5.6: Comparison of average y^+ values obtained with the base and refined meshes

A comparison between the outlet temperature and the pressure drop obtained with the base and refined meshes is conducted to evaluate the impact of mesh refinement on the predicted performance.

The predicted outlet temperature shows limited sensitivity to mesh refinement (Table 5.7). For all configurations, the variation remains below 2%, indicating that the overall thermal behaviour of the HEX is captured consistently by both meshes.

Config.	$T_{\text{out,base}}$ **[K]**	$T_{\text{out,ref}}$ **[K]**	**Diff.** [%]
C1	1365.641	1349.3582	-1.2
C2	1241.817	1219.983	-1.8
C3	1272.1964	1282.6199	+0.8

Table 5.7: Comparison of outlet temperature predictions obtained using the baseline and refined meshes

Instead, the predicted pressure drop remains more sensitive to mesh resolution. Depending on the configuration, the pressure drop decreases by approximately 13–17% with the refined mesh (Table 5.8).

Config.	Δp_{base} **[Pa]**	Δp_{ref} **[Pa]**	**Diff.** [%]
C1	56389.63	46875.96	-16.9
C2	95292.06	83126.86	-12.8
C3	165865.49	137969.15	-16.8

Table 5.8: Comparison of pressure drop predictions obtained using the baseline and refined meshes

This higher sensitivity is due to different physical mechanisms involved. Pressure losses depend on the wall shear stress, which is directly linked to the velocity gradients near the wall [24]. In helical channels, secondary flows modify the near-wall velocity distribution and make pressure-drop predictions particularly sensitive to the near-wall mesh resolution [14]. In contrast, the outlet temperature depends on the overall energy transferred to the fluid throughout the HEX. It is therefore less sensitive to local mesh variations. For these reasons, refining the mesh has a stronger impact on the predicted pressure drop than on the outlet temperature.

Chapter 6

Conclusions and Outlook

6.1 Summary of the Work

This thesis focused on the preliminary design and CFD assessment of a helical-tube HEX for the hydrogen-fuelled STT developed within the Green SWaP project.

The objective of this work was to identify geometrically feasible HEX configurations capable of heating the propellant from 300 K to at least the target temperature of 1130 K, while maintaining acceptable pressure losses.

To achieve this, using a near-1D thermal model, a MATLAB-based configuration-selection tool was developed to explore the design space of helical channel HEX configurations.

The preliminary model was used to evaluate the thermal and hydraulic performance of each configuration. Engineering constraints, followed by Pareto-based screening and local refinement, were applied to reduce the design space.

The most promising HEX configurations were then assessed through three-dimensional steady-state CFD simulations.

The main outcomes of the study are discussed below by answering the three research questions defined at the beginning of the thesis.

Q1 How do the main geometric parameters of a helical-tube HEX (number of tubes, tube inner diameter, and helix pitch) affect its thermal and hydraulic performance in a hydrogen-fuelled STT?

The effect of the number of channels depends on the selected channel diameter. For small diameters, the outlet temperature increases as the number of channels increases, because the larger heat-transfer area has a stronger effect on the thermal performance. For larger diameters, a non-monotonic behaviour was observed. In these cases, increasing the number of channels initially lowers the Reynolds number and the convective heat-transfer coefficient, causing a slight reduction in outlet temperature. However, as the number of channels continues to increase, the larger heat-transfer area compensates for this effect and the outlet temperature starts to rise again. Increasing the number of channels also tends to reduce pressure losses. Since the total mass flow rate remains constant, a larger number of channels reduces the mass flow rate through each channel, resulting in lower flow velocities, lower Reynolds numbers, and consequently lower hydraulic losses.

The effect of the helical pitch depends on the overall thermal effectiveness of the configuration. The difference in outlet temperature between the minimum and maximum pitch cases becomes smaller as the number of channels increases and the channel diameter decreases. This indicates that the role of the pitch is less important when the HEX already provides a large heat-transfer area and effective convective heat transfer. Under these conditions, changes in channel length have only a limited effect on the overall thermal performance of the HEX. On the other hand, the hydraulic influence of the pitch remains significant, since a smaller pitch increases the developed channel length and the pressure drop.

Q2 Which HEX configurations can be identified as promising design candidates after applying the Green SWaP thermal requirements and the imposed hydraulic and geometric constraints?

The most promising HEX configurations were identified through the combined use of design constraints, Pareto analysis and local design-space refinement. The Pareto analysis highlighted a limited region of the design space where outlet temperature and pressure losses were well balanced. This region was then investigated in more detail through a local refinement of the design variables. The selected candidates were generally characterized by relatively high numbers of channels and intermediate channel diameters, providing enough heat-transfer area to reach the target outlet temperature while maintaining acceptable pressure losses and geometric feasibility. The results also showed that the highest thermal performance does not necessarily correspond to the most favourable design. Instead, the most promising configurations were those able to satisfy the thermal requirement without introducing excessive hydraulic penalties.

Q3 To what extent do three-dimensional CFD simulations support the thermal and hydraulic performance trends predicted by the preliminary design methodology?

For the investigated configurations, the CFD assessment confirmed the main thermal trends predicted by the preliminary design methodology. This demonstrates the effectiveness of the approach for early-stage design exploration and candidate selection.

The two approaches supported the same pressure-drop trend. However, the hydraulic predictions showed larger differences in the absolute pressure-drop values. This suggests that pressure losses are more sensitive to modelling assumptions and numerical resolution.

Overall, the results show that the preliminary methodology is a useful tool for screening and identifying promising regions of the design space. CFD simulations are still needed for a more detailed assessment of quantitative pressure-drop predictions.

6.2 Limitations of the Proposed Approach

The main limitation of this work is the steady-state assumption adopted in both the preliminary design methodology and the CFD simulations. The analyses were performed assuming a constant wall temperature of 1400 K, without considering the gradual depletion of the thermal energy stored within the TES material. Instead, in a real STT, the wall temperature would decrease as thermal energy is transferred to the propellant, leading to a reduction in outlet temperature and thruster performance.

A second limitation is the thermal boundary conditions adopted in the CFD model: a spatially uniform wall temperature of 1400 K was imposed. As a consequence, simulations are insensitive to the local solar heat flux distribution, and local temperature variations or potential hot-spots within the structure could not be captured.

6.3 Future Perspectives

Future work should first focus on the development of transient CFD simulations capable of coupling the hydrogen flow with the thermal response of the TES material. This would provide a more realistic representation of the thermal depletion process and make it possible to evaluate how thermal performance evolve during the firing phase.

Future work should also investigate the discrepancy between the preliminary hydraulic predictions and the CFD results. Further CFD studies should include additional mesh refinement and higher-fidelity numerical analyses of additional CFD cases to better quantify the pressure losses within the HEX.

From a design perspective, CFD analyses suggest that pressure losses may become a limiting factor for conventional helical-channel HEXs. Future research should explore alternative architectures enabled by AM, such as TPMS structures. These geometries could offer larger heat-transfer areas while reducing pressure losses, making them attractive candidates for future STT applications.

Finally, a test campaign will validate the numerical results obtained in this work: experimental testing of additively manufactured prototypes would provide useful information on thermal-hydraulic performance, helping improve the proposed design methodology.

Bibliography

[1] George P. Sutton and Oscar Biblarz. *Rocket Propulsion Elements*. en. 9th ed. John Wiley and Sons, 2016 (cit. on pp. 1–3, 5, 10, 22, 26).

[2] Riccardo Cambertoni, Leonardo Dall'Osto, Angelo Cervone, Lily Blondel-Canepari, Alberto Sarritzu, Fabio Faraoni, and Angelo Pasini. «In-Orbit Reusable Kick-Stage Enabled by a Sustainable Space Mobility Solution Harvesting Solar Energy for Onboard Fuel Production». en. In: *The 76th International Astronautical Congress (IAC 2025)*. 2025 (cit. on pp. 1, 7, 17, 19).

[3] Fangzhou Song et al. «Feasibility analysis of solar thermal propulsion system with thermal energy storage». en. In: *Advances in Space Research* 71.5 (Mar. 2023), pp. 2493–2508 (cit. on pp. 2, 16, 17).

[4] Matthew R Gilpin. «High Temperature Latent Heat Thermal Energy Storage to Augment Solar Thermal Propulsion for Microsatellites». en. PhD thesis. Los Angeles, CA: University of Southern California, Aug. 2015 (cit. on pp. 3, 5, 13, 15–17).

[5] F G Kennedy. «Solar Thermal Propulsion for Microsatellite Manoeuvring». en. PhD thesis. Guildford, United Kingdom: University of Surrey, Sept. 2004 (cit. on pp. 3, 5, 6, 13, 15).

[6] Alberto Sarritzu, Lily Blondel-Canepari, Fabio Faraoni, Riccardo Cambertoni, Leonardo Dall'Osto, Angelo Cervone, and Angelo Pasini. «From Water & Sunlight to Thrust: New Propulsion Technologies within the Green Swap Project». en. In: *th International Astronautical Congress* (2025) (cit. on pp. 3–7, 17, 19).

[7] Faraoni Fabio, Sarritzu Alberto, and Pasini Angelo. «Performance Assessment of an H2O2/H2 Bipropellant Thruster for Innovative Water-based Space Propulsion». en. In: (2025), 16 pages (cit. on pp. 3–5, 7).

[8] Angelo Pasini et al. «Converting Water into Performant Propellants for In-Space Propulsion: Overview of the GreenSWaP project». en. In: *the International Astronautical Congress*. 2025 (cit. on pp. 4, 5, 7).

[9] James M. Shoji. *Beamed Energy Propulsion* (cit. on pp. 5, 13–15).

[10] Minchao Huang, Jianjun Wu, Jian Li, and Yuqiang Cheng. *Solar Thermal Thruster*. en. Singapore: Springer Nature Singapore, 2025 (cit. on pp. 5, 6, 11, 14, 18).

[11] Haoran Zhang, Minchao Huang, and Xiaoping Hu. «Heat exchange structure design and overall performance analysis of double-concentrator solar thermal thruster». en. In: *Acta Astronautica* 199 (Oct. 2022), pp. 277–292 (cit. on pp. 8, 18).

[12] James M. Shoji. *Solar Rocket Component Study*. en. Tech. rep. AFRPL-TR-84-057. Canoga Park, CA: Rockwell International, Rocketdyne Division, Feb. 1985 (cit. on pp. 13, 18).

[13] Andrew Michael Fsadni and Justin P.M. Whitty. «A review on the two-phase heat transfer characteristics in helically coiled tube heat exchangers». en. In: *International Journal of Heat and Mass Transfer* 95 (Apr. 2016), pp. 551–565 (cit. on p. 18).

[14] R.J. Fazzari, C.P. Marcel, and V.P. Masson. «Single-phase heat transfer prediction in helical coiled tubes in turbulent regime». en. In: *Nuclear Engineering and Design* 417 (Feb. 2024), p. 112870 (cit. on pp. 18, 69).

[15] Daniel Turner, Robert Howie, and Phil Bland. «The Development of a Next-Generation Latticed Resistojet Thruster for CubeSats». en. In: *Aerospace* 11.9 (Aug. 2024), p. 714 (cit. on p. 18).

[16] F. Romei and A. Grubisic. «Numerical study of a novel monolithic heat exchanger for electrothermal space propulsion». en. In: *Acta Astronautica* 159 (June 2019), pp. 8–16 (cit. on p. 18).

[17] Mohamed G. Gado et al. «Triply periodic minimal surface structures: Design, fabrication, 3D printing techniques, state-of-the-art studies, and prospective thermal applications for efficient energy utilization». In: *Energy Technology* (2024) (cit. on p. 19).

[18] Riccardo Cambertoni, Leonardo Dall'Osto, Angelo Cervone, and Stefano Speretta. «Additive Manufacturing Solutions for Solar Thermal Propulsion: An Integrated Core Design Approach». en. In: 2026 (cit. on pp. 19, 25, 26, 28, 30).

[19] J. B. Pearson, D. B. Landrum, and C. W. Hawk. «Parametric Study of Solar Thermal Rocket Nozzle Performance». en. In: *Journal of Solar Energy Engineering* 118.3 (Aug. 1996), pp. 194–195 (cit. on p. 26).

[20] Roland Winston et al. *Nonimaging optics*. Elsevier, 2005 (cit. on p. 26).

[21] Sanford Gordon et al. *Computer program for calculation of complex chemical equilibrium*. Reference publication. NASA, 1994 (cit. on p. 30).

[22] Jae-Young Choi, Jangho Park, Seulgi Yi, Yeongmin Jo, and Seongim Choi. «Design by adaptive infill sampling with multi-objective optimization for exploitation and exploration». en. In: *Probabilistic Engineering Mechanics* 67 (Jan. 2022), p. 103175 (cit. on p. 42).

[23] Shigeru Obayashi, Shin-Kyu Jeong, Koji Shimoyama, Kazuhisa Chiba, and Hiroyuki Morino. «Multi-Objective Design Exploration and its Applications». en. In: *International Journal of Aeronautical and Space Sciences* 11.4 (Dec. 2010), pp. 247–265 (cit. on p. 42).

[24] Frank P. Incropera and Frank P. Incropera, eds. *Fundamentals of heat and mass transfer*. en. 6th ed. Hoboken, NJ: John Wiley, 2007 (cit. on pp. 47, 69).

[25] Ramesh K. Shah and Dušan P. Sekulic. *Fundamentals of Heat Exchanger Design*. 2003 (cit. on p. 47).

[26] Nicholas C. Lopes, Yang Chao, Vinusha Dasarla, Neil P. Sullivan, Mark A. Ricklick, and Sandra K. S. Boetcher. «Comprehensive Review of Heat Transfer Correlations of Supercritical CO2 in Straight Tubes Near the Critical Point: A Historical Perspective». en. In: *Journal of Heat Transfer* 144.12 (Dec. 2022), p. 120801 (cit. on p. 47).

[27] Dennis Nikitaev, Corey Smith, and Kelsa Palomares. «Comparison of Convective Heat Transfer Correlations and Their Application to Nuclear Thermal Propulsion Reactors». en. In: *Nuclear and Emerging Technologies for Space (NETS-2022)*. Cleveland, OH: American Nuclear Society, 2022, pp. 696–705 (cit. on p. 47).

[28] Hao Zha, Yaqian Xu, Zhigong Tang, Bin Li, and Dongzhi Wang. «Conjugate Heat Transfer Advancements and Applications in Aerospace Engine Technology». en. In: *Applied Sciences* 14.9 (Apr. 2024), p. 3556 (cit. on p. 51).

[29] *Fluent 6.1 User's Guide*. Fluent Inc. 2003 (cit. on pp. 53–55, 59).

[30] Viviana Ferretti, Matteo Sciarra, Daniele Liuzzi, and Daniele Drigo. «3D Conjugate heat transfer model for simulation of Heat Transfer by High Roughness Cooling Channels». en. In: *the 9th European Conference for Aeronautics and Space Sciences (EUCASS)*. Lille, France, June 2022, 10 pages (cit. on pp. 53, 54).

[31] David C. Wilcox. *Turbulence Modeling for CFD*. 3rd. La Cañada, California: DCW Industries, Inc., 2006 (cit. on p. 54).

[32] Ansys, Inc. *Ansys Fluent User's Guide: 36.2. Choosing the Spatial Discretization Scheme*. Ansys Help. 2024 (cit. on p. 59).